Title
Visualization of Morphogenesis through Dynamic Instability Studies in 4-D printing

Author
Song, Jiaqi

Publication Date
2019

Peer reviewed|Thesis/dissertation

UNIVERSITY OF CALIFORNIA

Los Angeles

Visualization of Morphogenesis through Dynamic Instability Studies in 4-D printing

A thesis submitted in partial satisfaction of the

requirements for the degree Master of Science

in Materials Science and Engineering

by

Jiaqi Song

2019

ABSTRACT OF THE THESIS

Visualization of instability during morphogenesis

through 4-D printing

by

Jiaqi Song

Master of Science in Materials Science and Engineering

University of California, Los Angeles, 2019

Professor Ximin He, Chair

Abstract

Morphogenesis is the generation process of specific morphologies of living organisms depending on complex biological, biochemistry and mechanical process. Researchers have put effort on these interesting morphology formation based on artificial materials and applied them to the electrical devices, clinical applications and etc. However, few researcher achieved longitudinal buckling formation on the 3D surface which is similar to the patterns appeared on cucurbitaceous fructification (such as pumpkin). Recently, theoretical calculation and simulation model, for example spherical core-shell structure and tubular structure, are employed to explain the mechanism, yet they are lack of experimental validation. The heterogeneities of growth rate and mechanical property in these researches are considered as the most significant factors in

fabricating distinct morphologic formations. In this work, we demonstrate that longitudinal buckles of pumpkins can be reproduced by a barrel core-shell structure using 4D printing, which takes advantages of digital light processing (DLP) 3D printing and stimulus-responsive materials. The mechanical mismatch between the stiff core and compliant shell results in buckling instability on the surface. The initiation and formation of buckles are governed by the ratio of core/shell radius and the differences in swelling ratio and stiffness of the core and shell. We are capable of control the number of buckles increasing from 4 to 44 by simply tuning the swelling ratio of the shell. This heterogeneous structure with controllable buckling geometrically and structurally resembles the morphology of cucurbitaceous fructification and can be further applied to 3D anti-counterfeiting technologies. The heterogeneity mechanism in this work is also used to achieve different other morphologies like bending, helix and curving.

Keywords: morphogenesis, 4D printing, heterogeneous structure, instability

The thesis of Jiaqi Song is approved.

Yahong Xie

Yu Huang

Ximin He, Committee Chair

University of California, Los Angeles

2019

Table of Contents

List of Figures

List of Tables

Acknowledgement

First of all, I would like to thank my advisor, also the chair for this thesis, Professor Ximin He. She offered me great opportunity to work on this project, which has profound impact on my following research career. The ideas she shared with me, as well as unique perspective she has on each and every research project, inspire me to have creative experimental designs. Besides, she is patient and loves to discuss with me about problem I met in my research. Thanks for the guidance and encouragement that enable my completion of this thesis!

Second, I would like to thank my committee members, Professor Yahong Xie and Professor Yu Huang. Thanks for kindly review this thesis and offering your precious comments on it!

Last but not least, I would like to thank all the members from He's Lab. These members are not only my friends, but also my family. They will always show up for me when I feel down and help me out. Also thank Dong Wu, Mutian Hua and Zirui Zhai for the contributions in this work!

1. Introduction

1.1 4D Printing

1.1.1 Definition of 4D Printing

Recently, 3D printing technologies are quite mature to print complicated structures, thus researchers turned to the field of smart materials that can be manipulated in 3D printing, leading to the existence and development of 4D printing. In 2013, 4D printing was first introduced as a brand new concept by research group from MIT.[1] As shown in Figure 1.1(a), their 3D printed rod could automatically shift to the shape "MIT" in seconds.[3] Figure 1.1(b) illustrates the first 4D printing paper on shifting printed sheet into complex structure using active materials.[2] Inspired by these two works, 4D printing started to attract many researchers' attention.

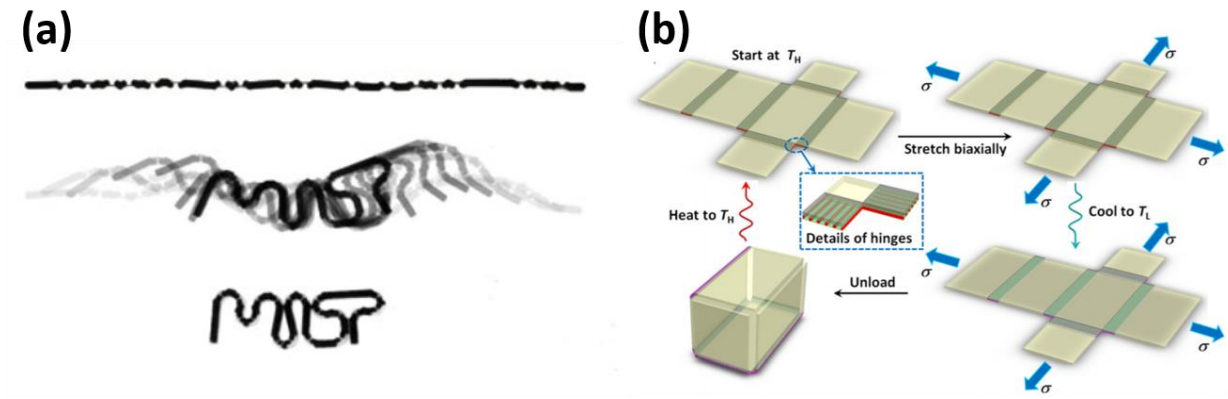

Figure 1.1 (a) 3D printed responsive rod transformed into "MIT" according to the programmed design. Reproduced with permission.[3] Copyright © John Wiley & Sons Ltd; (b) Shape memory sheet turned into a hollow box. The process is also called origami. Reproduced with permission.[2] Copyright © 2013 AIP Publishing LLC.

We can simply consider 4D printing as transformation of 3D printing objects with respect to time,[3] yet the scope of 4D printing is not as narrow. 4D printing nowadays refers to the shape

shifting, property transformation and functionalization of 3D printed active materials when the sample meets with the corresponding stimuli, such as water[4,16], heat[26,27], light[28,29] and pH[30]. The research scope includes 3D printing technology, fast responsive materials and simulation of the materials functionalization which we consider it the basic mechanism underlying the transformation.

In short, two principles must be fulfilled before we define one process a "4D printing process". First, the printed objects are expected to be responsive to stimuli and their movements are predictable according to the previous design. Second, there need to be stimuli to drive the objects to make the transformation or functionalization appear.

1.1.2 Significance of 4D Printing

4D printing has several advantages compared with traditional 3D printing. As discussed above, the printed materials are stimuli-responsive according to the required design so that they can be fabricated as soft robots. Also, 3D printing has issues with printing complex hollow structures whereas 4D printing are capable of shifting simple 2D structure into designed 3D structure, which casts down the waste of raw materials and the printing time.[5] What's more, shape shifting feature enabling facile storage for the materials since the objects are not a 3D structure anymore, but a 2D thin film. Figure 1.2 illustrates areas that 4D printing technology are applied: origami, smart devices, smart packages, metamaterials, biomedicine and tissue engineering.[7,8] 4D printing has important contributions being applied to electrical devices, clinical application and many other prospective research fields.

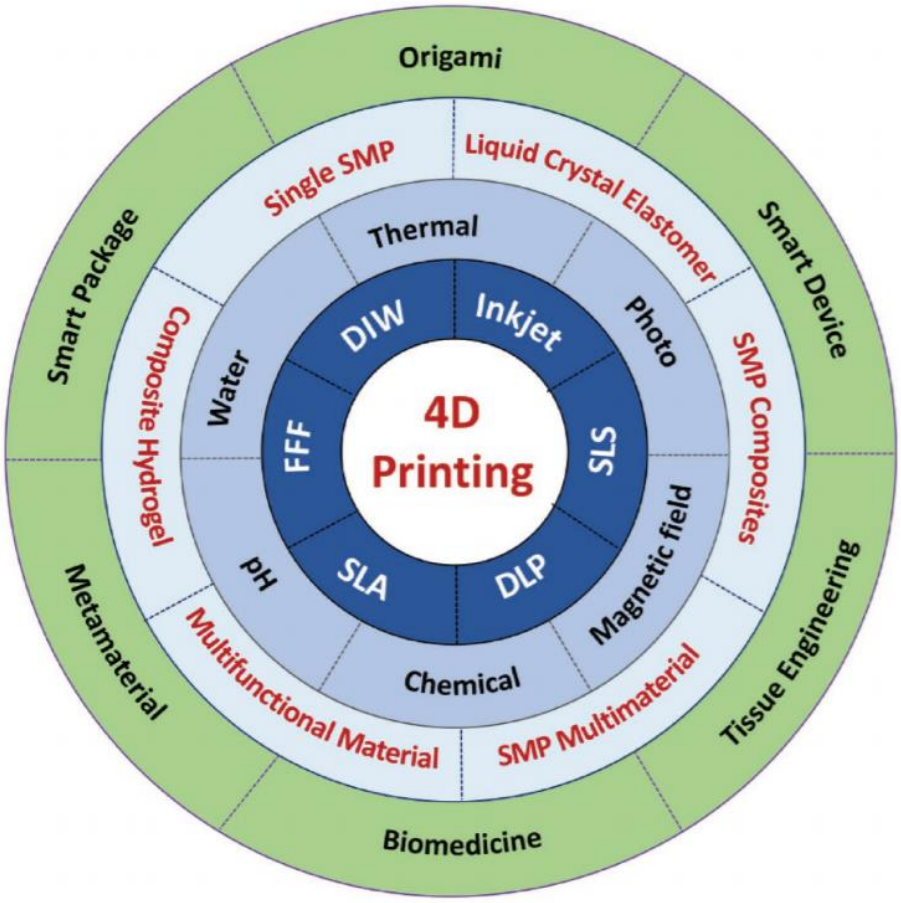

Figure 1.2 The categories of 4D printing are shown. From inner circle to outer circle: 1) 3D printing technology: Inkjet printing, fused filament fabrication (FFF), direct ink writing (DIW), stereolithography (SLA), digital light processing (DLP) and selective laser sintering (SLS); 2) The stimulus for active materials. 3) Active materials compatible for 4D printing. 4) 4D printing applications. Reproduced with permission.[6] Copyright © 2018 WILEY-VCH Verlag GmbH.

1.1.3 Digital Light Processing (DLP)

Among all 3D printing technologies, digital light processing is commonly used to print hydrogel and shape memory polymers. DLP replies on a digital micromirror device for dynamic

pattern generation.[6,21] Here, the dynamic pattern means the continuous patterns that are applicable to print a complex structure. Usually, narrow band width UV light can be used as light source to initiate photocuring. As illustrated in Figure 1.3, UV light source came from the imaging unit which is usually a commercial projector, and reflected by the optical mirror, finally reaches the precursor resin. In order to control the precision of height of printing layers, researchers applied oxygen or photo-absorber to inhibit polymerization. As the support plate quickly went up, continuous changing images resulted in complicated structures.[6,22-23] High resolution (micro- and nanoscale) DLP can be achieved with optical lens systems (called projection micro-stereolithography (PμSL)).[23-25] What's more, multi-material DLP is realized by applying switchable vats[38] or grayscale light[39-42].

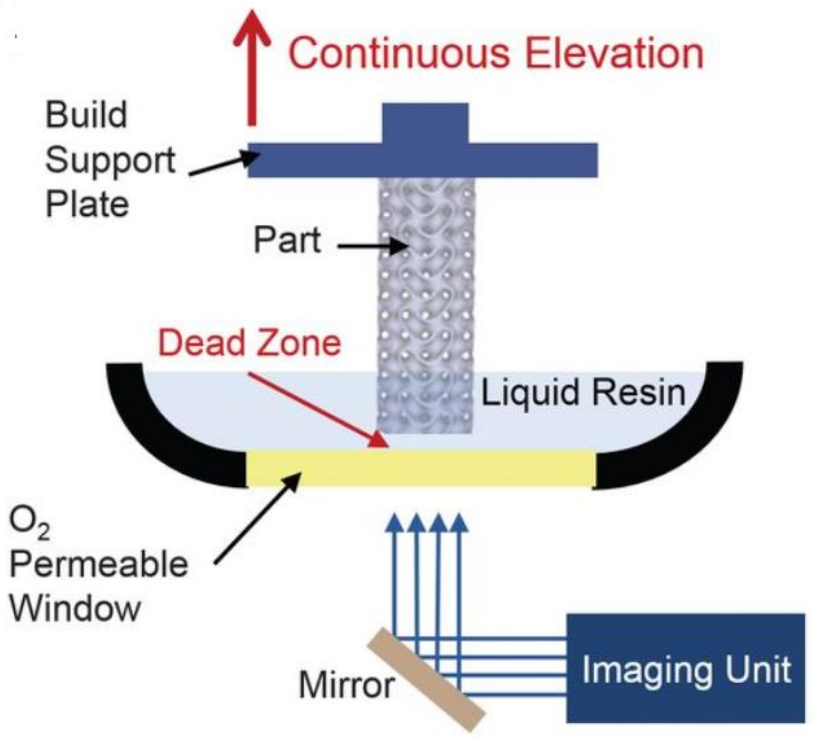

Figure 1.3 Schematics of precise digital light processing with oxygen as the inhibitor to increase the resolution. Reproduced with Permission.[23] Copyright © The American Association for the Advancement of Science.

1.2 Biological Morphogenesis

1.2.1 Definition of Morphogenesis

Different species distinguish from one another by their unique morphologies. For example, pumpkins have vertical groovy structure all around the surface to increase the anti-bending capability; brain has wrinkles onside to increase the specific surface area for larger load of information management. While the embryonic development of each specie / organ starts with similar profile during the growth process, different morphologies, especially their surface patterns and textures, are eventually developed in the matured state across many length scales. Ubiquitously for example, centimeter scale cortical convolutions and groovy patterns on fruits, millimeter scale fingerprints, and even micrometer scale features like buckled tumor surface and crumpled membrane of white blood cells. This phenomenon is termed as morphogenesis. Basically, morphogenesis refers to the whole emerging process of specific morphologies for different species. As the synergistic result of complicated biological, biochemical and mechanical processes, morphogenesis in the biological system is yet fully understood. Therefore, this unique yet common phenomenon is still of great importance and interest to biologists, materials and mechanics scientists.

1.2.2 Mimicking Morphogenesis of Bauhinia Pods Helix

Helix formation[9,10,36,37] appears over the plants' stem and leaves, among which Bauhinia pods helix are widely and analyzed achieved morphogenesis. The real Bauhinia pods is shown in Figure 3.13. Wu et al.[9] printed heterogeneous responsive hydrogel to achieve helix

morphogenesis under ion solution. They printed a thin sheet with fiber-like regions which show different responsiveness under stimuli. They applied multistep curing method to print the structure. First, they photo-cured a poly(N-propylacrylamide) (PNIPAM) hydrogel sheet onto the substrate, and then they apply photomask to shine extra UV light on the fiber-like regions to cure poly(2-acrylamido-2-methylpropane sulfonic acid) (AMPS) and PNIPAM composites. Submerged in ion solution, PNIPAM is under ion-dehydration process whereas PAMPS shows water retention, thus the shrinkage of the fibers was smaller than other regions and caused helix. As illustrated in Figure 1.4(a), printed sheet formed helix when the temperature reaches 45℃. The wavelength of the helix were controlled by the angle between lines and the long axis.

The helix morphology have potential clinical applications illustrated in Figure 1.4(b). Wei et al.[10] introduced magnetic iron oxide into thermo-responsive shape memory polymers and realized remote control of helix deformation. Magnetic iron oxide is capable of generating heat under changing magnetic field and the heat triggered the deformation of shape memory object. Since the penetration of the magnetic field is quite well through the human body, it is possible to remotely control the helix deformation inside the vessel (if compressed helix was set inside the vessel previously) and make the helix an intravascular stent.

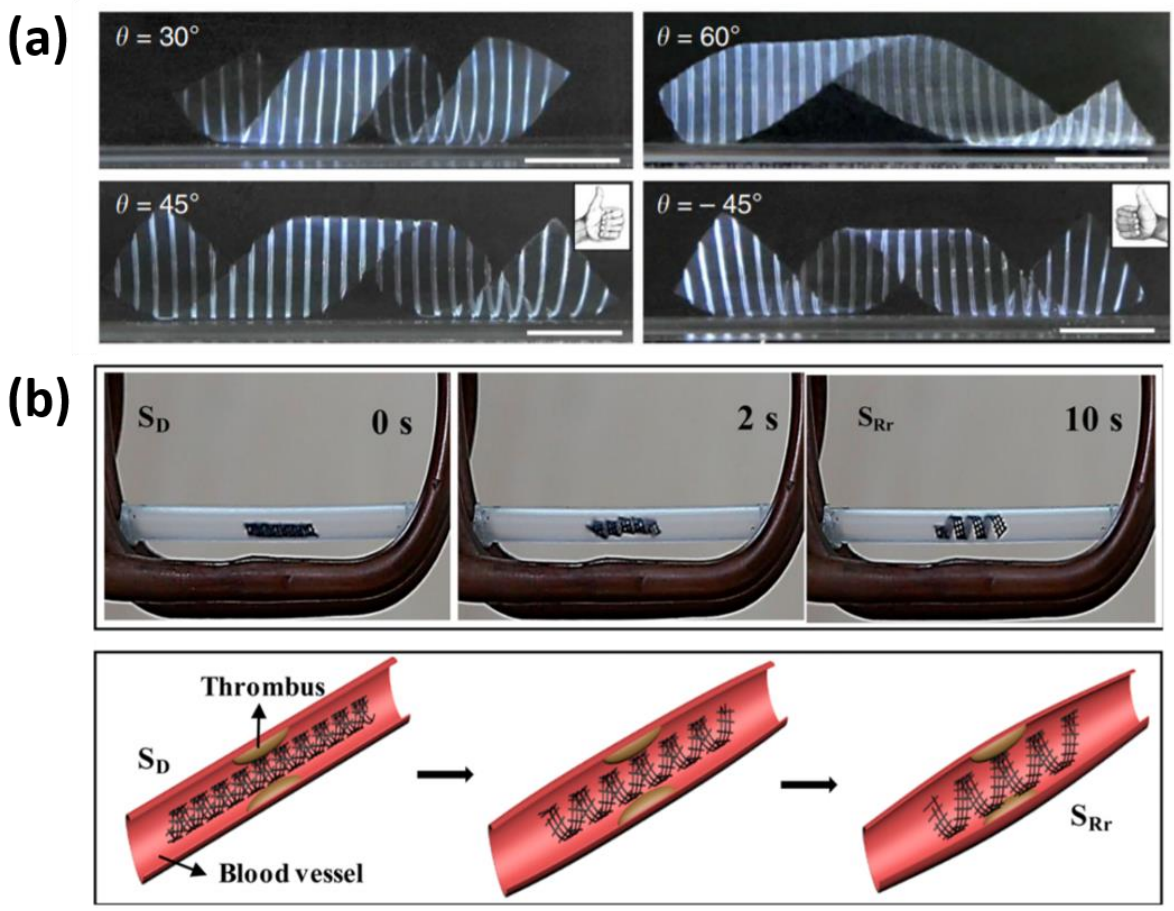

Figure 1.4 (a) The helix generated when PAAM-PAAM/PAMPS gel submerged in 1M NaCl solution for 1 day. The angle was between fiber region and the long axis. Reproduced with permission.[9] Copyright © 2013 Nature Publishing Group. (b) Remote control of helix deformation as intravascular stent inside vessel. Reproduced with permission.[10] Copyright © 2017 American Chemistry Society.

1.2.3 Mimicking Morphogenesis of Flower Blossom

Among all the biological morphogenesis, flower blossom morphogenesis attracts most attention from researchers.[11,16,28,34,35] Wu et al.[11] printed multi-layer model with different cross-linking density to realize blossom as illustrated in Figure 1.5(a). Higher cross-linking density hydrogel will contain less solvent (acetone) molecules, thus when the stiff layer meets with water, slower desolvation results in less shrinkage; while lower cross-linking density hydrogel maintains loose network and contains large amount of acetone inside, the desolvation becomes faster. Based on the principle, each petal of the bud will bend towards low cross-linking density side and eventually blossom. They printed darker grey scale layer, i.e. the low cross-linking density layer, outside of each petal, which made petals bend outward and finally blossomed. Most of the researches controlled simple blossom morphogenesis based on the double- or multi-layer model. More complex flower morphology was realized by Gladman et al. They reported hydrogel based biomimetic flower architectures including a native orchid and a native calla lily flower.[16]

The blossom process can be applied to the drug-eluting device in vivo.[12] In Figure 1.5(b) shows a gripper bended with heat stimuli. They cured rigid poly(propylene fumarate) (PPF) panels onto flexible thermal responsive poly(N-isopropylacrylamide-co-acrylic acid) (PNIPAm-AAc) hinges. Above 32 ℃ PNIPAm will shrink, thus the gripper closed and bended towards PNIPAm side; Below 32 ℃ PAAc will swell and the gripper closed towards the opposite direction. Multi-fingered structure facilitated its grabbing onto soft tissues and porous hydrogel network is applicable for drug release.

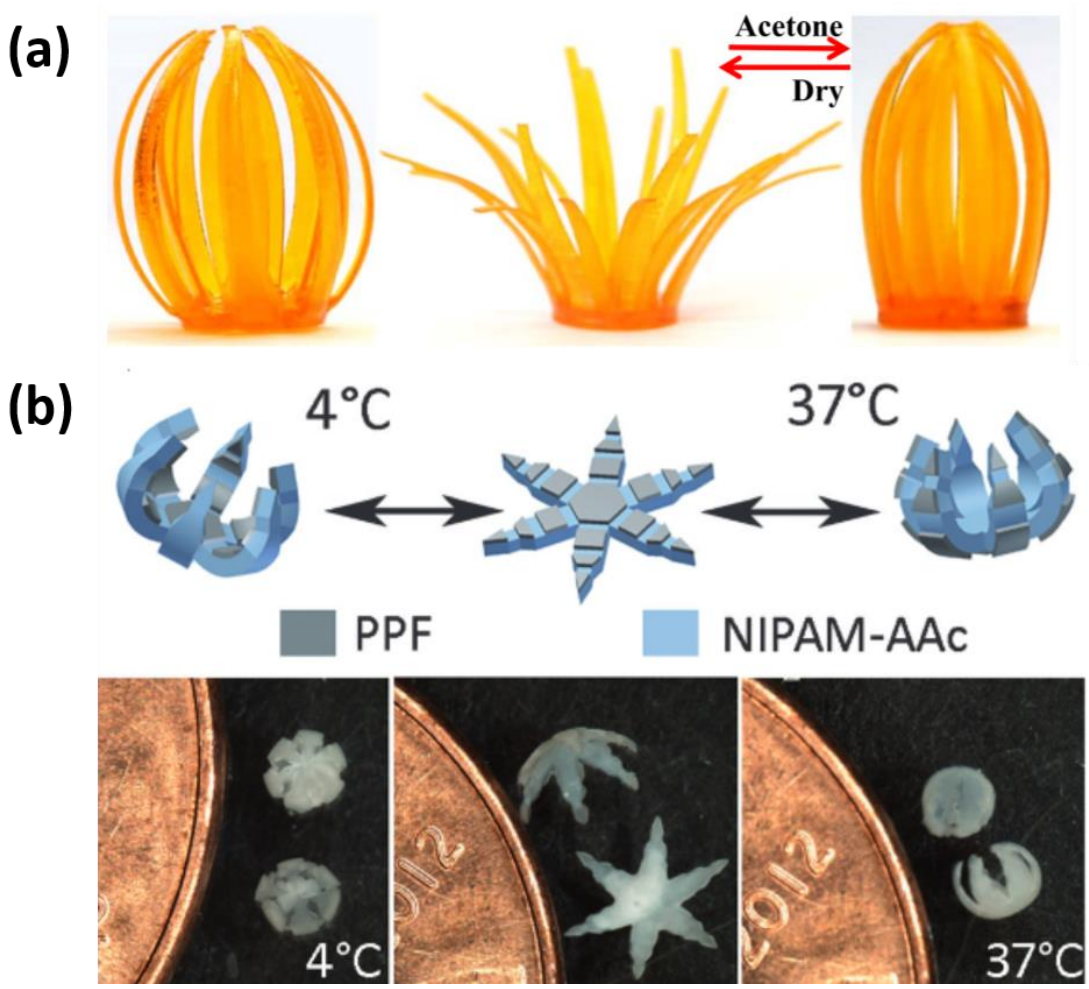

Figure 1.5 (a) Blossom of a printed heterogeneous flower: printed flower structure using grayscale light (outside of petals had darker grey scale and lower cross-linking denistry) blossomed after desolvation. Reproduced with permission.[11] Copyright © 2018 IOP Publishing Ltd. (b) grippers with rigid PPF panels on flexible stimuli-responsive PNIPAm–AAc hinges. Reproduced with permission.[12] Copyright © 2014 Wiley-VCH Verlag GmbH.

1.2.4 Mimicking Morphogenesis of Buckle Formation

To understand the complex process of buckle morphogenesis, extensive research and investigation have been conducted from the molecular, genetic and cellular perspective by biologists and botanists. Alternatively, other scientists take a more macroscopic approach by studying the phenomena on the basis of mechanics and mathematics, usually by the abstraction of the biological tissues into elastic or hyper-elastic material models and focus on the fundamental stress and strain development. Generally, different morphologies can be achieved via the formation of various mechanical instabilities patterns during external loadings. The surface of the material would keep smooth until the applied compressive stress exceeds a critical value. Upon surpassing the threshold, buckling would occur on the surface of the material, characterized by the sudden localized deflection of surface. To maintain the minimized free energy, undulation patterns will gradually develop across the surface of the material with the build-up of stress field.

Based on the conventional instability theories, various analytical calculations and Finite element analysis models have been developed to explain the origin of different buckle morphologies during morphogenesis as shwon in Figure 1.6. Chen et al. has reported a quantitative mechanics framework of stress-driven anisotropic buckling on model spheroidal shell/core (film/substrate) systems. They approximated various natural fruits and vegetables as spheroidal stiff exocarp (shell)/ compliant sarcocarp (core) system, which exhibit intriguing buckling profiles.[13] Dervaux et al. has studied the circumferential deformation of a free hyperelastic disk mimicking the growth of a green algae.[14] Suo et al. has investigated the creases formation of soft tissue growing inside a rigid shell or outside a rigid core.[15]

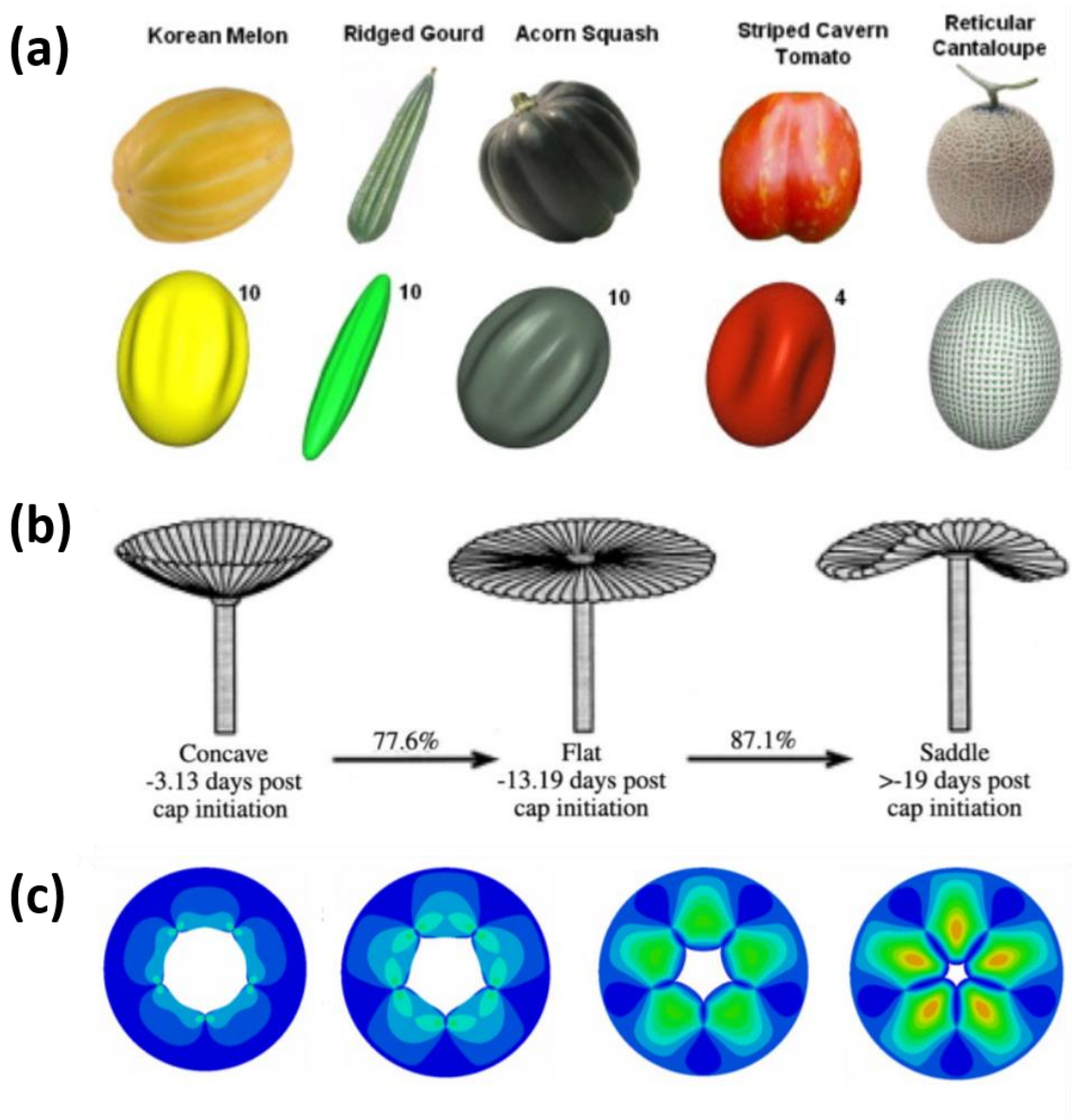

Figure 1.6 (a) Implications for fruit morphogenesis: the morphologies of several fruits and vegetables are compared with the simulated buckle shapes of model spheroids. Images on top are real fruits and those on bottom are simulation results. Reproduced with permission.[13] Copyright © 2019 Elsevier Ltd. (b) Shape changes in the Acetabularia algae. Reproduced with permission.[14] Copyright © 2008 The American Physical Society. (c) Deep creases develop from the surface of a tube of a tissue growing inside a rigid shell. Different numbers of creases are prescribed. Reproduced with permission.[15] Copyright © 2011 EPLA.

To aid the theoretical development, active/responsive materials, which undergo volume and/or property changes in response to environmetal stimulus has been utilized for experimental validation of morphogenesis models. For example, in Figure 1.7(a), Ben Amar et al. utilized two different hydrogels with different swelling ratios to validate their model of shape transition in 2D melanoma.[17] 3D printing technology has also been adopted for the facile fabrication of the material models. The combination of 3D printing and responsive materials are often referred to as 4D printing, with time being the extra dimension. 4D printing technology has been widly used to achieve various morphologies and intelligent behaviors. In Figure 1.7(b), simple tubular hydrogel structures with one end fixed have been fabricated by using DLP 3D printing for the investigation of their buckling formation due to the instability.[18,19] The driving froce of their model is from the fixed end of the materials, yet not caused by the free expansion of the 3D structure. In Figure 1.7 (c), Tallinen et al. analyzed undulaton formation on a curved hemi-sphere surface and achieved different varieties of buckles mimicking the fold in real brain.[20] They applied double layer model (2D model) which contains swellable thin coating onside the hemi-sphere elastomer.

Few experimental study to date have been conducted on the morphogenesis process based on 3D heterogeneous materials models. Moreover, most reported 4D printed structures evolve from 2D flat sheets to 3D complex shapes but lacking study on direct transition on 3D subjects. Biological tissues are always complex in both 3D geometry and material composition, which inspired us to take advantages of 4D printing as a powerful tool to further study the complicated 3D morphogenetic mechanisms strated from various plants.

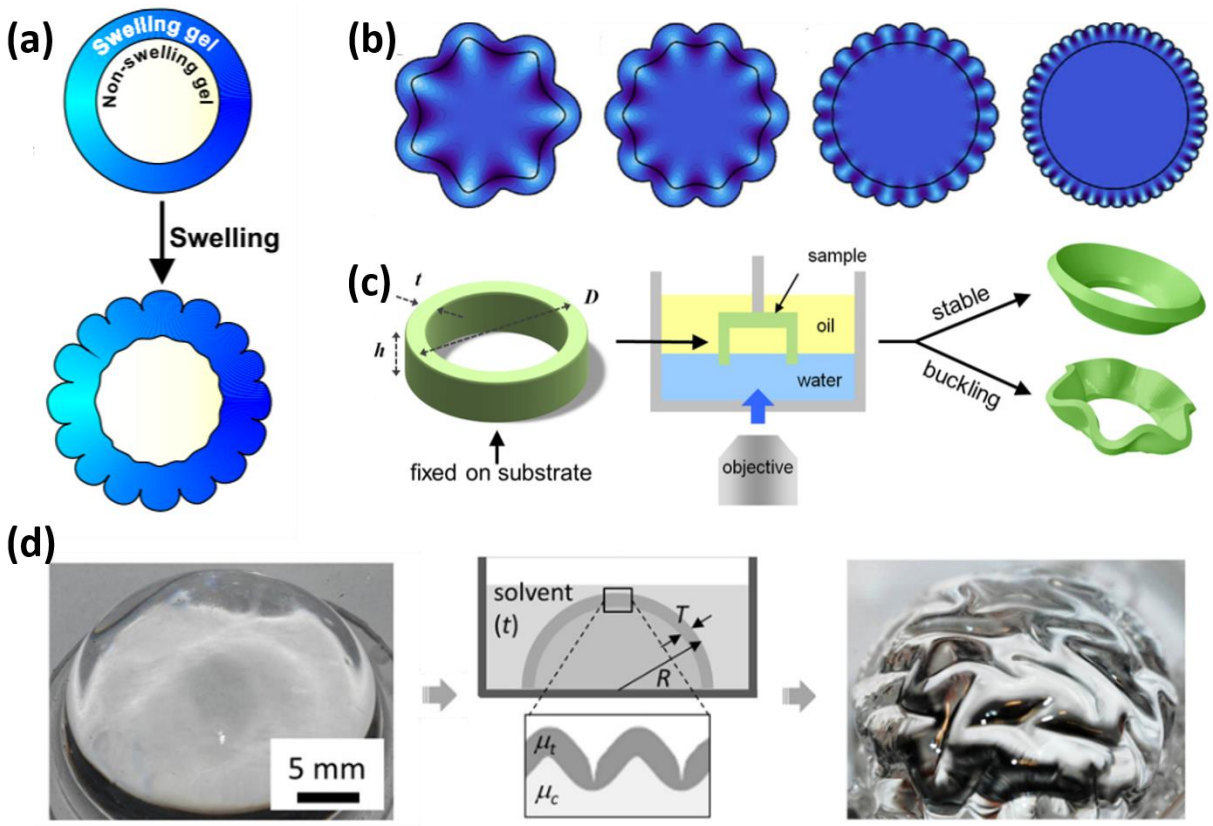

Figure 1.7 (a) Schematics of heterogenous hydrogel printing and swelling; (b) Various simulation results of buckle formation with similar aspect ratios=height of the cone/ diameter of the cone=0.13 and increasing values of stiffness of inner gel/stiffness of outer gel (from left to right: 0.25, 0.5, 1, 6). Reproduced with permission.[17] Copyright © 2011 American Physical Society. (c) Pattern formation by circumferential buckling of gel tube. Characteristic dimensions of tubular gel and experimental setup for 3D printing. Reproduced with permission.[18] Copyright © 2012 American Physical Society. (d) A physical model of brainlike instability. To mimic the growth of the gray matter in the brain, a hemispherical elastomer is coated with a top elastomer layer that swells by absorbing solvent over time. Representative images of a bilayer specimen in the initial state is shwon on the left and swollen state is shown at right. Reproduced with permission.[20] Copyright © 2014 The National Academy of Sciences of the United States of America.

1.3 4D Printing Biomimetic Morphogenesis in This Work

In this work, we combine digital light processing (DLP)-based 3D printing technology with stimuli-responsive hydrogels to 4D print a heterogeneous core-shell structure that geometrically and structurally represents the plant's organ. The materials model experimentally mimics the growing process of pumpkins upon swelling of the hydrogel to monitor morphology evolution and to understand the mechanism of such morphologic maturation. . In the model, the less swellable, stiff core emulates the central part of the fruit which consists of fibrous strands wrapping the seeds between two pole ends. The highly swellable, soft shell mimics the soft mesocarp of the fruit where growth is most significant. As the core and shell in one layer are printed continuously, the core/shell interface is seamlessly coherent.

We have achieved controllable modulus of the core and shell by simply control the curing time. The mismatch between the expansion and stiffness of the core and shell causes the compressive stress in the compliant shell and eventually leads to the buckling on the surface. The buckles firstly appear on the top of the structure and then develop to the entire surface. With the varying ratio of core and shell radius in one structure, a top-guide mechanism of 3D buckling growth is demonstrated. The ease of instability occurring to the top layers is corresponding to a previously reported theory that concentric-circles structures with thinner shell are more likely to form buckles. Besides, the rigid core in the structure also acts as confinement on the two polar ends, exerting compressive stress and inducing the buckle formation at top surface.

This work, for the first time, elucidates on the prerequisites, mechanisms, and the dynamic process of buckle formation of a 3D non-homogeneous self-confined object without external boundary, beyond the previous established bucking mechanism of 2D uniform object with

boundary confinement. Besides pumpkin, materials models of some other common plants were also established and corresponding artificial morphogenesis were achieved by 4D printing.

2. 4D Printing Procedure

2.1 Construction of the 3D Printing Platform (With Mutian Hua)

The printing was accomplished by a home-made DLP-based 3D printing system as shown in Figure 2.1. The system was composed of a PRO4500 UV light (385 nm) projector from Wintech Digital System Technology Corporation, a motorized translation stage mounted to a motor controller and other optical accessories from Thorlabs. A home-made program was used to realize the coordination control of the projection and the movement of stage. The resolution of the printer can achieve 30 μm on the x-y plane and 10 μm in the z-axis direction.

The reactive printing precursor is cured by UV light layer by layer to print the 3D structure. A 3D model was first designed which is a double layer barrel in our case. We can easily cut the 3D model into 2D slides series by Solidworks 3D CAD Software or we can simply draw series of slides through Microsoft Powerpoint. The patterns were projected by the UV projector on the stage which was immersed into the precursor solution. Since the printed structure was a core-shell barrel structure, the patterns projected on the substrate consisted of a small circle and a lager one for each layer. Within each printing layer, a lager circle was first projected for a shorter curing time (3-4s) and it will serve as our soft shell; followed by the projection of the small circle pattern at the center for a longer curing time (10s) to form the stiff core. Once a layer was printed, the support plate would move down allowing the projector to print another layer upon the top of the printed structure. For all the samples with core-shell structure, 50 layers were printed. The thickness of each layer was set to 0.1 mm. After the printing completed, the sample was rinsed in ethanol to get rid of the unreacted components and redundant photo absorber. Since the materials we print is a hydrogel, thus the network can be expanded with the existence of

water molecules as shown in Figure 2.1.

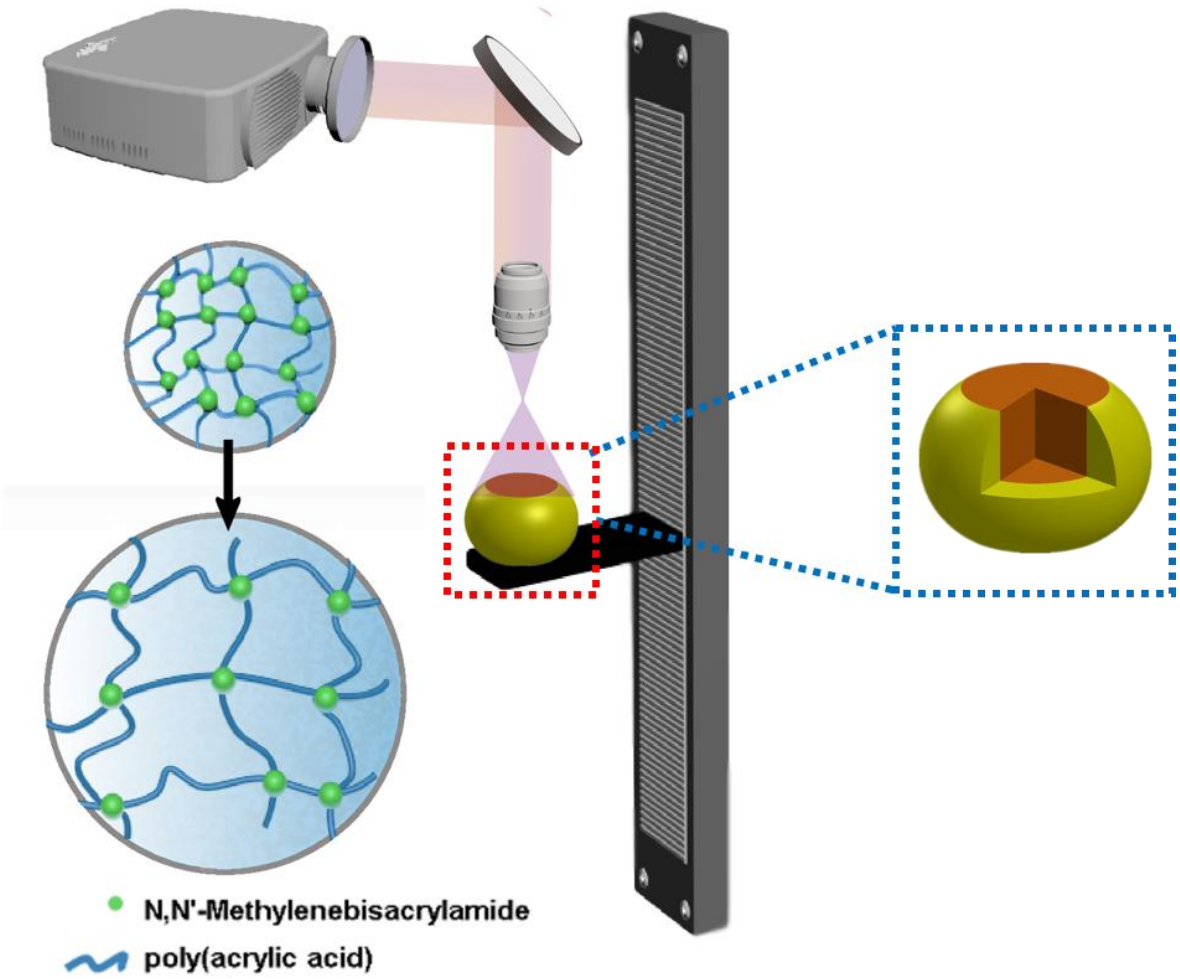

Figure 2.1 Schematic of projection micro-stereolithography system. A 385nm projector projects an exemplary core-shell based barrel on a substrate immersed in the photo-reactive precursor. Polymers are simultaneously produced and settled on the substrate layer-by-layer.

2.2 Principle of the 4D Process and Morphogenesis in This Work

As mentioned in the Introduction section, 3D printable active materials are commonly used in

the fabrication of reversible origami, morphologically controlled surface pattern, soft robotics, etc. As a typical stimuli-responsive material, hydrogel can undergo drastic volumetric change in response to various environmental stimuli, such as pH, temperature and humidity. Notably, the swelling ratio and mechanical performance of hydrogels are usually controllable by tuning the chemical composition and the structure of the network. The hydrogel network is capable of expanding during the swelling process and its swelling ratio is mainly determined by the crosslinking density of the polymer network. Here, we utilize a poly (acrylic acid) (pAAc) hydrogel as our printed active material and take advantage of its swelling behavior to realize the 4D procedure. PAAc hydrogel shows faster responsiveness to water and ions, comparing with other hydrogels like poly acrylamide (pAAm), thus we chose it as our target material.

Since the structures were printed layer by layer, the outlines of each layer can be clearly observed as shown in Figure 2.2(c), these inevitable horizontal circumferential lines exist as layers are printed. Although these lines are trivial to the 4D process, we do not want readers to be distracted by the noise. By controlling only one parameter, the curing time, we are able to print hydrogel with different swelling ratio and stiffness, which allow us to fabricate heterogeneous 3D hydrogel structures. *(Detailed analysis will be discussed in Section 3)* What we want to realize is vertical buckles formation directly on the 3D surface which few researcher has achieved in experiments. We chose pumpkin as our model because Cucurbita species happen to coordinate with similar morphogenesis our materials are expected to achieve. With this approach, we 3D printed a baby pumpkin-like heterogeneous 3D hydrogel structure with a stiff core and a soft shell and hopefully it can grow into a groovy large pumpkin only with the stimuli of water.

Figure 2.2(a)-(c) respectively illustrate a real pumpkin growing process, the variation of a pumpkin model, and a real evolution of our printed hydrogel structures in the buffer solution. In

the Initial State, the as-printed core-shell sample consists of a long-curing-time core (marked as orange in the model) and a short-curing-time circumferential shell (marked as yellow). This printing profile generates a soft shell with large swelling ratio and a stiff core which swells less. The surface of the hydrogel structure is smooth without buckle at the beginning. As it was immersed in water, molecules started to diffuse into the hydrogel networks and therefore, the networks expanded over time. The structure started to grow through a transition state. After around 3 hours, trivial creases appeared on the surface at the two polar ends of the structure. Eventually, the barrel will grow into a pumpkin-like structure. In this buckled state, large and regular buckles can be observed on the surface of structure after 4 hours immersion in the buffer solution. These longitudinal buckles start from one end of the sample to the other. With the evolution of this swelling structure, we successfully mimicked the morphogenesis of pumpkin, which starts with a barrel-like baby pumpkin and ends up with a ripe pumpkin with ribs.

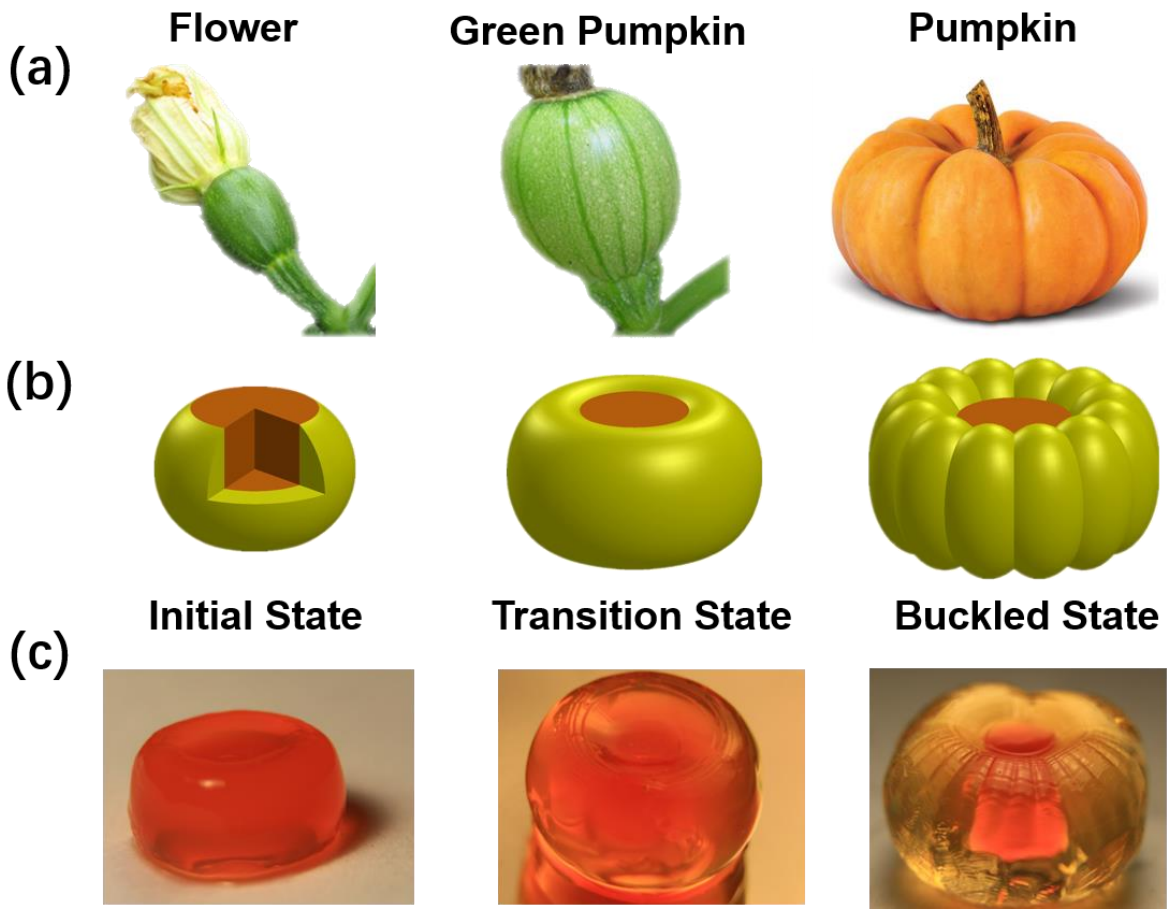

Figure 2.2 (a) growth of pumpkin and (b) corresponding schematic diagram and (c) pictures of the printed hydrogel structure during the swelling process.

2.3 Precursor Preparation

2.3.1 Materials

Acrylic acid (AAc), N,N'-methylene-bis-acrylamide (Bis), Sudan I dye andIrgacure-819 (phenylbis(2,4,6-trimethylbenzoyl)phosphine oxide)were purchased from Sigma-Aldrich, Inc. Dimethyl sulfoxide (DMSO) solvent, ethanol and pH 7.00 dihydrogen potassium phosphate-sodium phosphate dibasic buffer solution were purchased from Fisher Scientific Inc., All chemicals were used without further purification and treatment.

2.3.2 Precursor Preparation

To prepare the precursor solution for the 3D printing process, acrylic acid as the monomer; N,N'-methylene-bis-acrylamide as the crosslinker, Sudan I dye as photo absorber, Irgacure-819 as photo initiator were mixed in DMSO solvent. The mixture was vortexed and then ultrasound treated for 10 minutes to achieve a clear reddish precursor solution. Besides, ethanol was used for rinsing the samples and pH 7.00 dihydrogen potassium phosphate-sodium phosphate dibasic buffer solution was used as swelling agent for the printed hydrogels.

3. Control and Mechanisms of 4D Process (With Dong Wu)

The previous researches usually use a spheroidal structure with a stiff thin shell and compliant core to explain the formation of the pumpkin's morphology.[43] In this work, we proposed a different core-shell structure to realize the ordered buckling on the surface. As demonstrated in Section 2, we are capable of realize this unique formation in experiment by printing swellable barrel with soft shell and stiff core. To have some insight of the mechanism of the buckle formation, we conduct following experiments to prove the structure is necessary for buckle growth and explore the underlying factors that effect the whole process.

3.1 Simple Control Experiment

A control trail was firstly conducted to prove the significance of the heterogeneity: one sample was printed with 10s-cured core and 3s-cured shell, the other, as the control group, was a homogenous sample with 10s curing per layer. Except the printing image for two samples are different, number of the layers, diameter of the cylinder and the rinse time in ethanol and water for two samples are the same. As shown in Figure 3.1(a), after swelling in water, the blank group without core-shell structure does not generate buckles on the surface and the whole surface remains smooth; while in Figure 3.1(b), the core-shell barrel forms 4 buckles which can be obviously observed from the side view and the top view of the model. Researchers name these buckles, which generate from the top of the model all the way to the bottom, vertical buckles or longitudinal buckles. The red color was caused by Sudan I and it will not influence the swelling process of the hydrogel. This control experiment proved the heterogeneity and the mechanical mismatch between core and shell are the major incentive for the surface patterning of the structure.

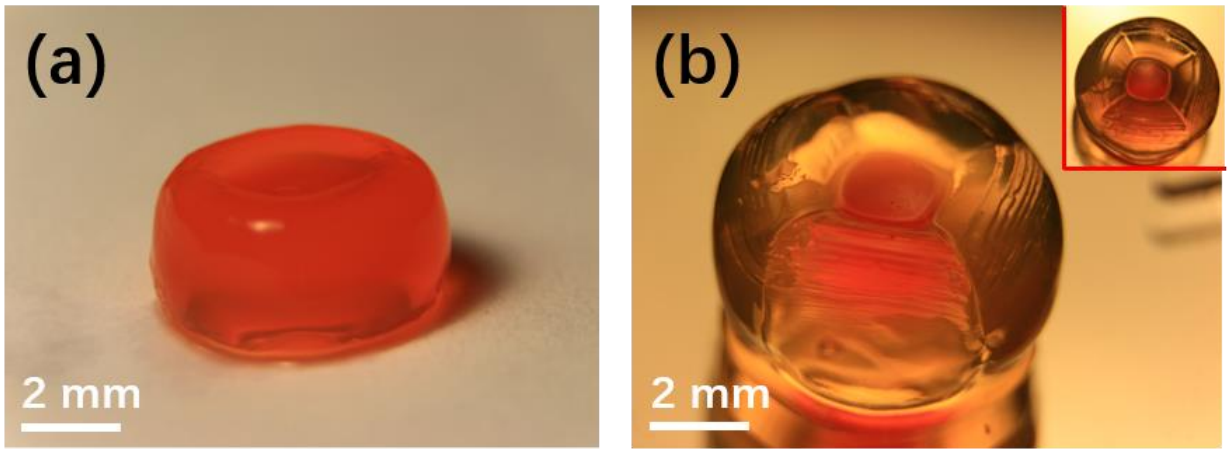

Figure 3.1 (a) homogeneous structure with 10s curing time for each layer of the hydrogel and (b) heterogeneous structure with 3s-cured shell and 10s-cured core (bottom).

3.2 Properties for Core and Shell in the Model

Next set of experiments is to analyze the difference between the core and shell since only core-shell structures can generate large buckles on the cylindrical surface. It is clear that we are capable of tuning the curing time to control the properties of the printed active materials and the primary difference between core and shell is the curing time, thus we investigated how swelling ratio and stiffness of the materials related to the curing time of printing process.

3.2.1 Tune Swelling Ratio with Different Curing Time

Thin discs of gels with diameters of 2.1 cm and thickness of 2 mm were printed with various curing time to measure the swelling ratios. As printed, the samples were first rinsed with ethanol to wash away the unreacted monomers and dyes. Then they were put into pH 7 buffer solution to swell for 6 h. The changes of the discs' diameters through time were measured to calculate the swelling ratios. Here we define the swelling ratios as the ratio of instantaneous diameters to the

initial diameters of the discs.

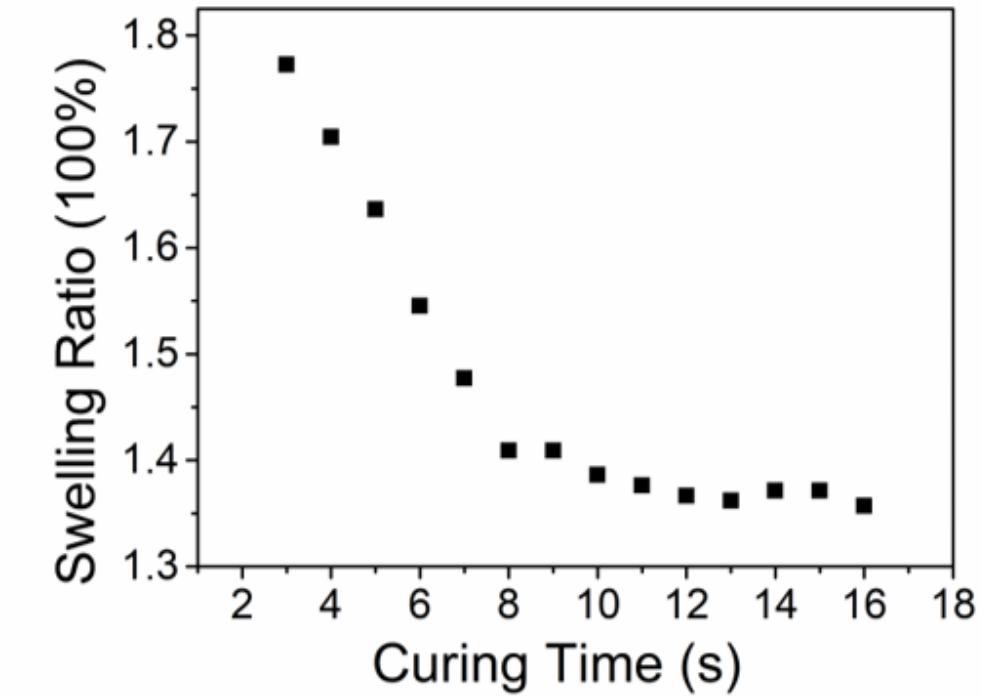

Figure 3.2 Swelling ratio of disks with respect to curing time. Each point in the plot refers to one disk sample with different curing time and the swelling ratio is measured after submersion in buffer solution for 6 hours.

We printed homogeneous hydrogel discs with different curing time and measured their diameter variation after immersion in buffer solution for the same period of time. The relation between curing time and swelling ratio is plotted in Figure 3.2. As curing time increases, the swelling ratios first decrease and eventually becomes stable. One important information from the plot is that the difference between swelling ratio from 8s cured sample and 16s cured sample is relatively trivial, thus we chose 10s as our less-swellable core. As for our soft shell, 3s cured sample and 4s cured sample are manipulated because of the significant swelling ratio. Specifically, samples with layer exposure time of 3s led to the discs increasing 77% in diameter

and reaching equilibrium state, while 38% for 10s-cured printed hydrogel using the same precursor.

3.2.2 Stiffness Variation with Different Curing Time (with Dong Wu)

To measure the Young's modulus of the printed hydrogels with different curing time, 15-layer samples with dog-bone shape were printed with various curing time (3 to 20 seconds per layer), rinsed with ethanol to get rid of unreacted monomers and extra dye and then dried in an oven. Dynamic Mechanical Analysis (DMA850) purchased from TA Instruments was used to measure the stress-strain curves of the printed samples. The moduli were obtained as the slope of the stress-strain curves.

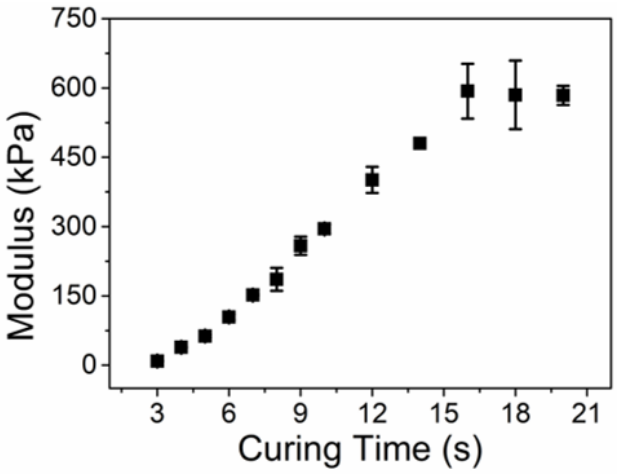

Figure 3.3 Stiffness of dog-bone samples with respect to curing time. Each point in the plot refers to one dog-bone sample with different curing time.

As plotted in Figure 3.3, modulus of the sample increases dramatically as the curing time for each layer increases. The modulus for 3s is around 8.9 kPa and for 10s is about 295 kPa, the contrast=(modulus of 10s cured hydrogel/modulus of 3s cured hydrogel)=33. Another reason we chose 10s cure core and 3s cure shell is that the stiffness contrast between 10s and 3s meets with

the buckle formation requirement and larger contrast will cause detachment problem between two layers.

3.2.3 Scanning Electron Microscope for Different Curing Time Sample

Scanning electron microscope (SEM) was used to study the microstructures of the printed samples. The SEM images are obtained by using ZEISS Supra 40VP SEM. To prepare the samples for SEM imaging, the gels were first immersed in the buffer solution until they fully swelled. Then they were frozen by using liquid nitrogen and left in the freeze dryer (Labconco corporation, Freezone 1L) overnight. After that, a layer of gold was sputtered onto the samples for the SEM imaging, using the PELCO®SC-7 auto sputter coater.

As shown in the SEM images in Figure 3.4, the pore size of the network is largely dependent on the curing time. Layers with exposure time of 3s showed pore size about 20μm while 10s exposure time produced hydrogel with pore size around 5μm. The SEM images is helpful to understand the swelling and mechanical property difference with respect to the curing time of the sample: Loose network for 3s cured hydrogel results in higher diffusion rate of water molecules from the environment to the polymer network, which causes the swelling ratio to be higher with same amount of submersion period; also the loose network leads to low mechanical property for the whole sample.

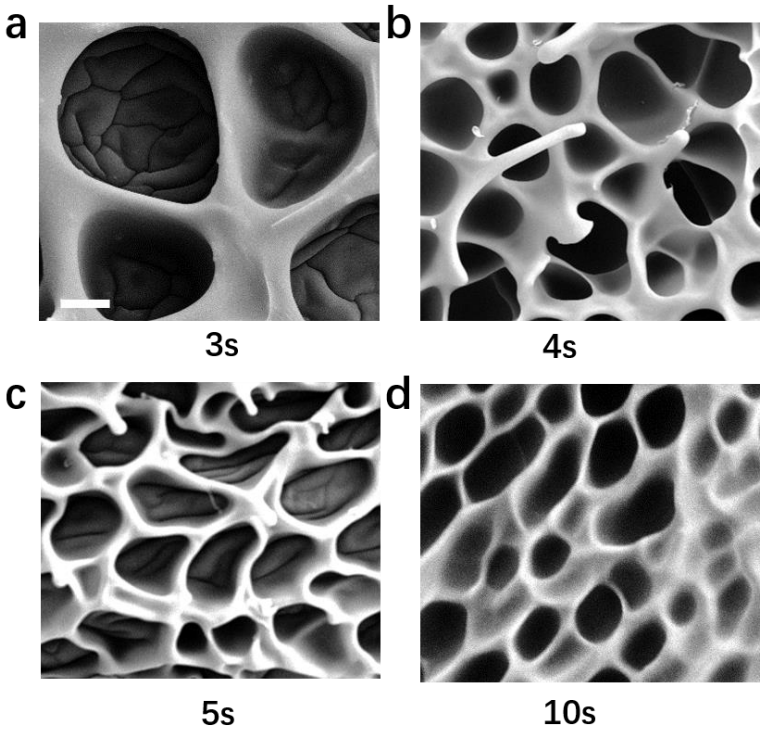

Figure 3.4 Scanning electron microscopy images of the microstructures in the hydrogels with different curing time (a) 3s, (b) 4s, (c) 5s and (d) 6s.

3.3 Buckle Control

With the understanding of hydrogel properties upon the curing time of each layer, we achieved buckle control. We took advantages of this core-shell model and printed samples with the same curing time for core yet different curing time for shell.

For the sample in Figure 3.5(a), we printed the shell 3s each layer while 10s each layer for the core. In order to make the sample more similar to baby pumpkins, we intentionally control the diameter of shell in each layer so that the profiles were printed barrel. After 4 hours immersion in pH = 7 buffer solution, samples generates large longitudinal buckles from top to bottom on the

surface of the structure as shown in Figure 3(b). The top view of the sample in Figure 3(c) allows us to observe the deep groove extend from the top core to the side surface.

To investigate the relation between the curing time and the buckle formation, we used the same printing model but changed the layer curing time of the shell to 3.5s and 4s. The initial and final states of the printed samples are shown in Figure 3(e)-(g) and (h)-(j). Compare the buckle density and numbers illustrates in Figure 3(b), (f) and (i), it shows that the so-generated buckle density and buckle number increases along with the increasing curing time for the shell, meaning stiffer and less swellable shell generates denser buckles. Figure 3(c), (g) and (j) illustrate more clear buckles shape and number from the top view, thus we can get average numbers of the buckle are 4 (3s-10s sample), 24 (3.5s-10s sample) and 44 (4s-10s cured sample). The results coordinates with our expectation since less swellable shell will generate buckles with higher density but lower amplitude. *(Detailed discussion will be in Section 3.4)* Figure 3(d)-(k) shows the simulated results of the cross-section of the middle layer of the structure, which has the similar trend of buckling formation as the experimental results. *(Detailed discussion will be in Section 3.5)*

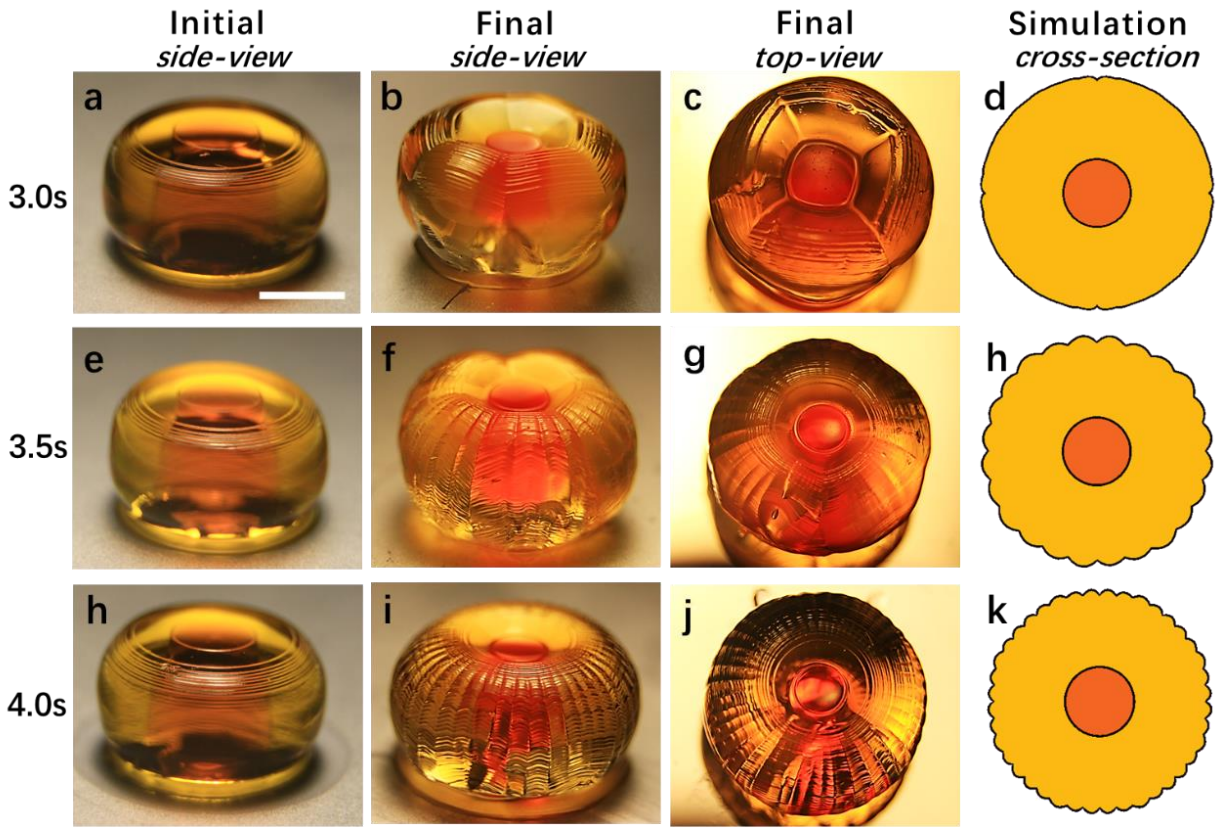

Figure 3.5 Initial state (a) (e) (h), final state side view (b) (f) (i) and top view (c) (g) (j), simulated results (cross-section) (d) (h) (k) of the printed structure with different shell curing time:3s, 3.5s, 4s respectively. (scale bar = 5mm)

3.4 Mechanism of the Buckle Formation

3.4.1 Threshold for Buckle Generation

In order to analyze the mechanism of the buckle formation to further control the number and amplitude of the buckles, we captured images for materials submerged in buffer solution once every hour. However, we found a threshold for buckle generation, before which the surface of the samples was smooth without buckle. Moreover, the buckle generation happens within 15

minutes after the threshold, thus we shortened the gap of formation capturing.

As shown in Figure 3.6, we immersed the samples in water and ethanol for 10 minutes alternatively. We chose 4s cured shell and 10s cured core as our sample so that more buckles can be observed on the surface. After 3 hours and 35 minutes of immersion, the sample did not have patterns onside (Figure 3.6 a), yet when we submerged this sample in buffer solution for 10 more minutes, the surface of the sample was covered with stable buckles (Figure 3.6 b). Additionally, when we put our sample into ethanol, which makes it to shrink, for 10 minutes, buckles disappeared and the surface return to the smooth state (Figure 3.6 c). We conducted reversible buckle forming and disappearing for 10 times and the number and the amplitude of the buckles did not alter much (Figure 3.6 d).

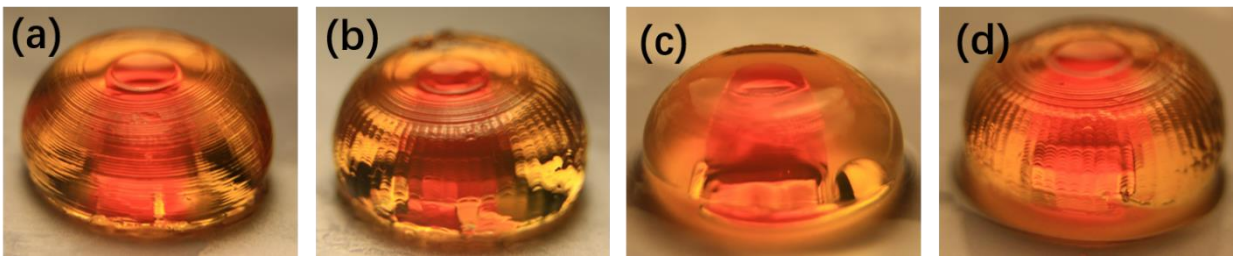

Figure 3.6 (a) Sample with 4s-cured shell and 10s cured core submerged in buffer solution for 3 hours and 35 minutes; (b) Same sample submerged in buffer solution for 3 hours and 45 minutes; (c) Sample turn back to smooth state after 10 minutes submersion in ethanol; (d) Sample after alternative submersion in ethanol and buffer solution for 10 times and finally maintained stable reversible buckles on the surface.

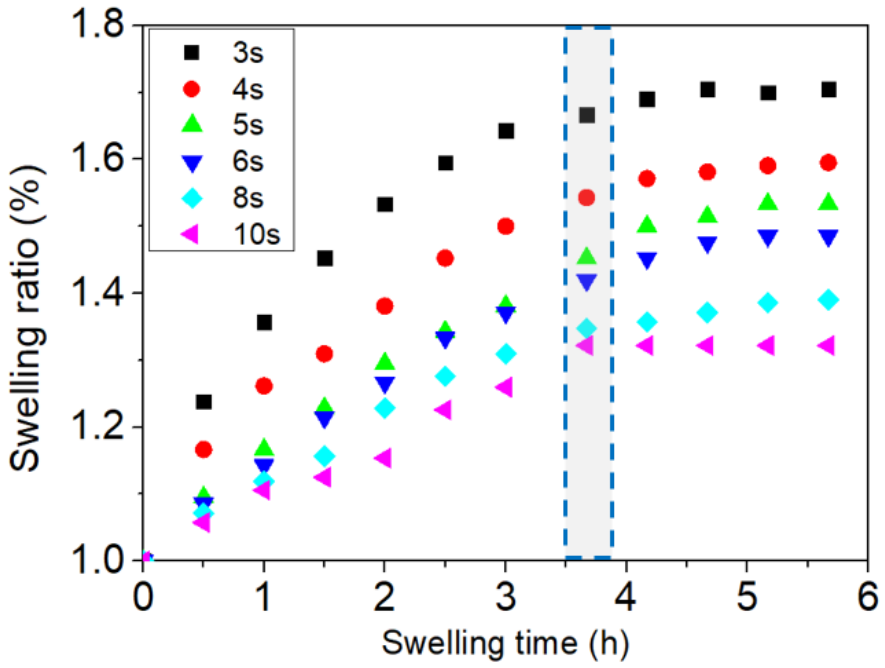

Figure 3.7 Swelling ratio of different curing time samples with respect to the swelling time. Grey area shows the buckle formation happens between 3h35m to 3h41m for the 4s-10s sample.

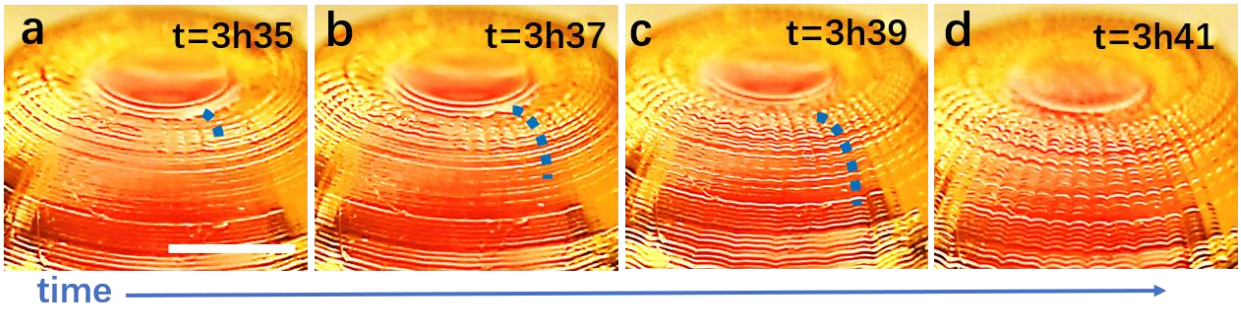

Figure 3.8 The buckles started to appear when the structure swelled to a critical level (a) and extended from the top to bottom (b) (c) and eventually covered the surface of the structure (d).

3.4.2 Avalanche Type Buckle Formation

With the awareness of the threshold and fast generation speed for the buckles, we analyzed the swelling behavior for the sample with submersion time between 3 hours 35 minutes and 3 hours

45 minutes. As shown in Figure 3.7, swelling ratio of different curing time samples with respect to the swelling time were plotted. The grey area in the illustration demonstrated the buckle formation period. Compared to Figure 3.2, this plot demonstrated the dynamic process for the pattern formation. It shows that the swelling rate of 4s cured shell is much faster than that of 10s-cured core, yet only when the swelling ratio reaches certain threshold value, this avalanche type buckle evolution will initiate. Specifically, when the hydrogel was under buffer solution for 3 hours 35 minutes, the swelling ratio for 4s-cured shell reaches 52% where the buckles started to appear as illustrated in Figure 3.8 (a). Then the buckle grew longer and eventually cover the whole surface of the shell shown in Figure 3.8(b), 3.8(c) and 3.8(d). The blue dashed lines are used to help identify the extension process. It is noteworthy that the buckling pattern quickly formed in 6 minutes, before which the surface was smooth without pattern onside.

3.4.3 Mechanism of the Fast Buckle Formation

As shown in Figure 3.9, we designed this printed pumpkin-like barrel to have longitudinal buckles on the curved profile. According to the theory of Jin et al.[4] the core-shell structure can be comparably easier to reach its instable state when the ratio of A/B is lager (A = the radius of core, B = the outer radius of the shell). That is to say, instability will firstly occur to the top layers with larger core/shell ratio in our printed structures, which is corresponding to our experimental results. As the structure continue to swell, the middle part of the structure soon reached the critical condition that buckles started to form on the surface. It is important to note that, the theoretical calculation predicted that the numbers of buckles should be different due to the varying core-shell ratio.

However, the experimental results showed the continuous buckles through the surface as the

extension of the buckles on the top, which indicates the significance of the interaction between each layer and the buckles formation at the top. This difference between theoretical and experimental results is mainly because that the gel system is not simply under a 2D stress state and as a consequence, the theoretical calculation will lose its accuracy in describing the dynamic process in the 3D object in experiment. Thus, we take the 2D buckling theory as a prediction of only the buckling trends but not the numbers of buckles.

Moreover, as the relatively less-swelling core prevents (confines) the free expansion of the high swelling-ratio shell, the compressive stress exerted by the stiff core on the soft shell also contributes to the buckles on the top ends. As the buckles first form at the top layers, it will induce the layers below to form buckles as the extension to relieve the stored energy caused by the instability to achieve an equilibrium state. As a result, the growth of buckles starting from the top to the whole surface can be observed as shown in Figure 3.9.

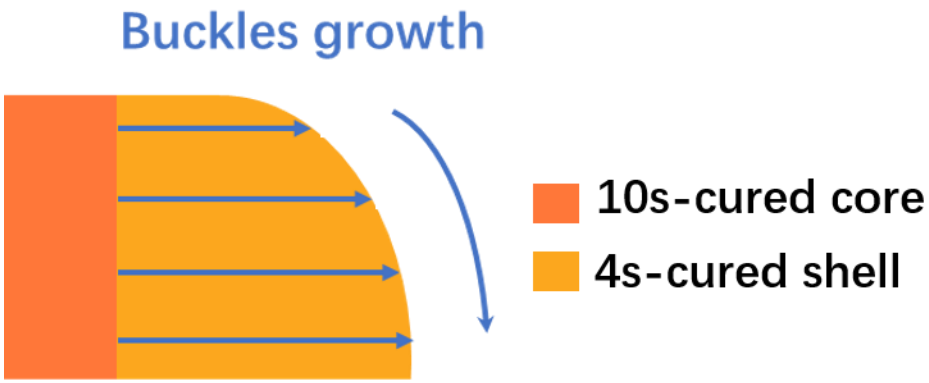

Figure 3.9 Schematic of the buckles' growth from top to equatorial plane.

3.5 Various 4D Processes

Besides the buckling of Cucurbita species, many other morphogenesis of fruits and vegetables

are widely observed in nature. These morphologic formations are usually attributed to the anisotropic growth of cells and tissues as well as the heterogeneous structures of the organisms. Here we applied the method of 4D printing to control the swelling ratios and the modulus in different parts of the structure, mimicking the morphogenesis of 4 different plants. We printed a core-shell thin disc structure as shown in Figure 3.10(a). The swelling mismatch between 3s-cured shell and 10s-cured core, after 2 minutes swelling in buffer solution, will lead to the formation of the cabbage leaf-like profile a as shown in Figure 3.10(b). We also achieved a flowering process by printing a heterogeneous double-layer 2D flower structure as shown in Figure 3.11(a)-(b). The different swelling ratio in responsive to water of the two layers allows the petals to act as a bilayer actuator bending to the center and mimicking the morphology of chrysanthemum. Besides core-shell structures and bilayer structures, distinguished morphologies of plants can also be induced by stiff thin lines in their structures. In Figure 3.12(a), we printed a leaf-shape structure with soft mesophyll and stiff vein inside. After immersion in buffer solution for 2 minutes, the printed leaf will turn into a curved profile as shown in Figure 3.12(b). In addition, a soft strip with a group of 45-degree inclined parallel stiff lines inside was printed and developed into a helix structure similar to Bauhinia pods, after immersion in buffer solution as shown in Figure 3.13(a)-(b). The simulations of the 4 different structures in Figure 5(c), (g), (k), (o) show corresponding results as the experimental ones. Real natural organisms are also shown in Figure 5(d), (h), (l), (p). With our 4D printing method, we can easily fabricate heterogeneous structures to mimic the morphogenesis or reproduce the morphologies of various plants.

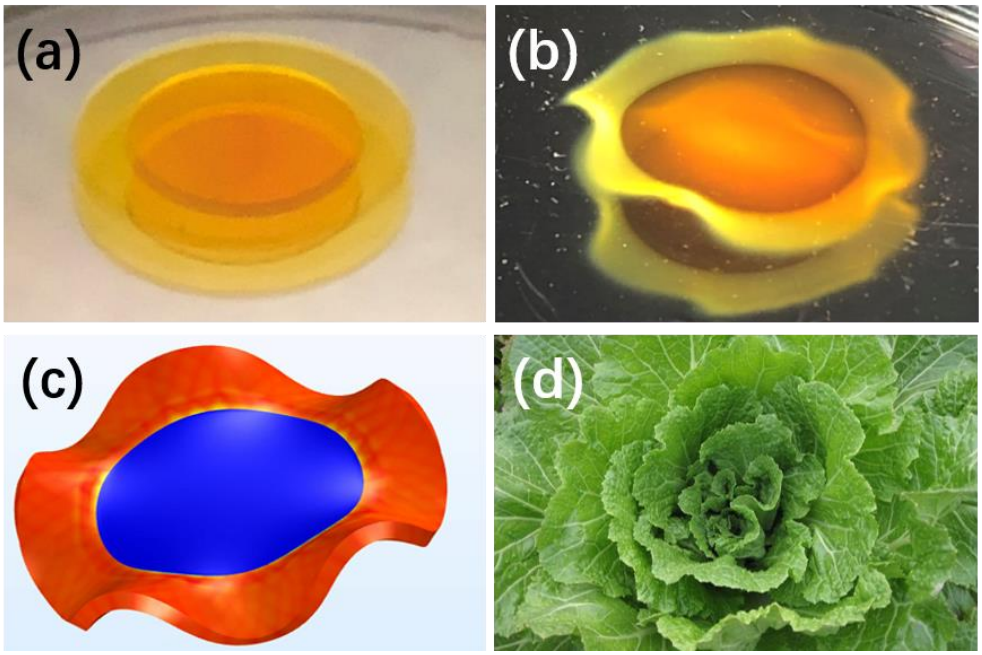

Figure 3.10 (a) the initial plain state; (b) the final buckling state; (c) the corresponding simulated models; and (d) the real images of cabbage flowers/leaves. (scale bar is 5mm)

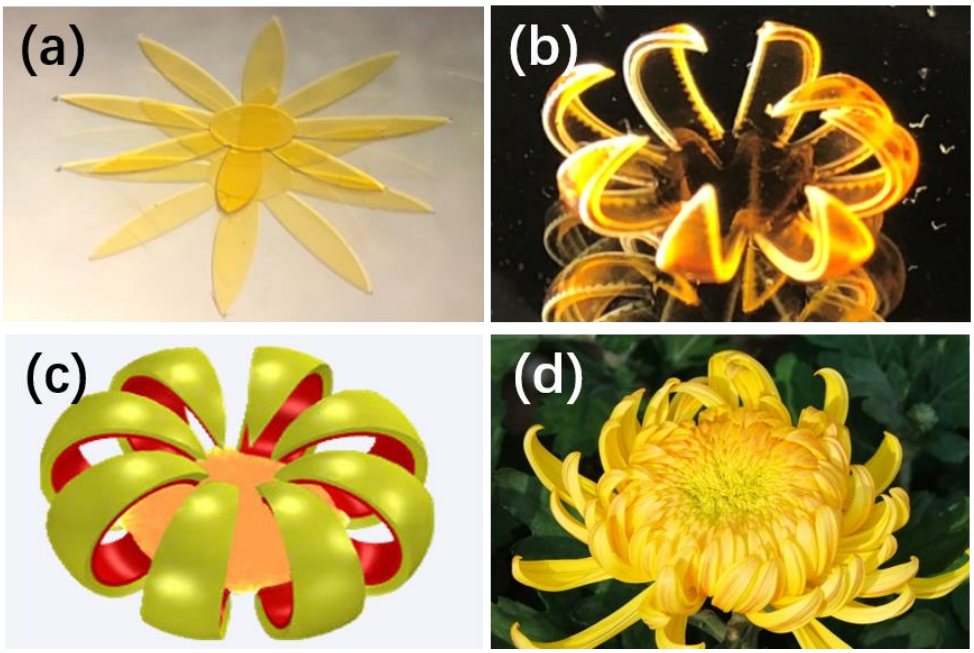

Figure 3.11 (a) the initial plain state; (b) the final buckling state; (c) the corresponding simulated models; and (d) the real images of chrysanthemum. (scale bar is 5mm)

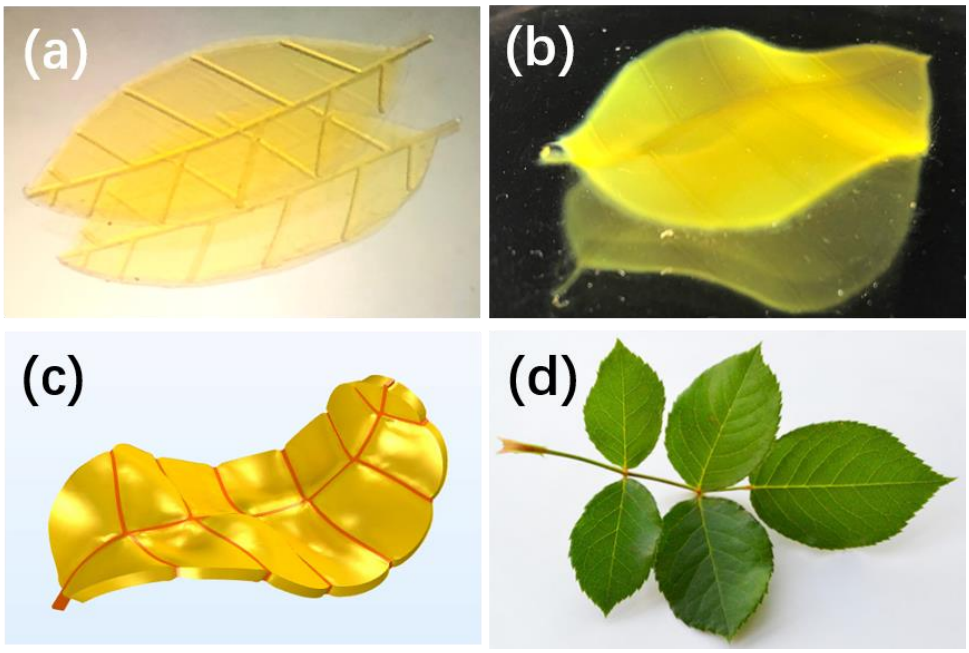

Figure 3.12 (a) the initial plain state; (b) the final buckling state; (c) the corresponding simulated models; and (d) the real images of leaves of rose. (scale bar is 5mm)

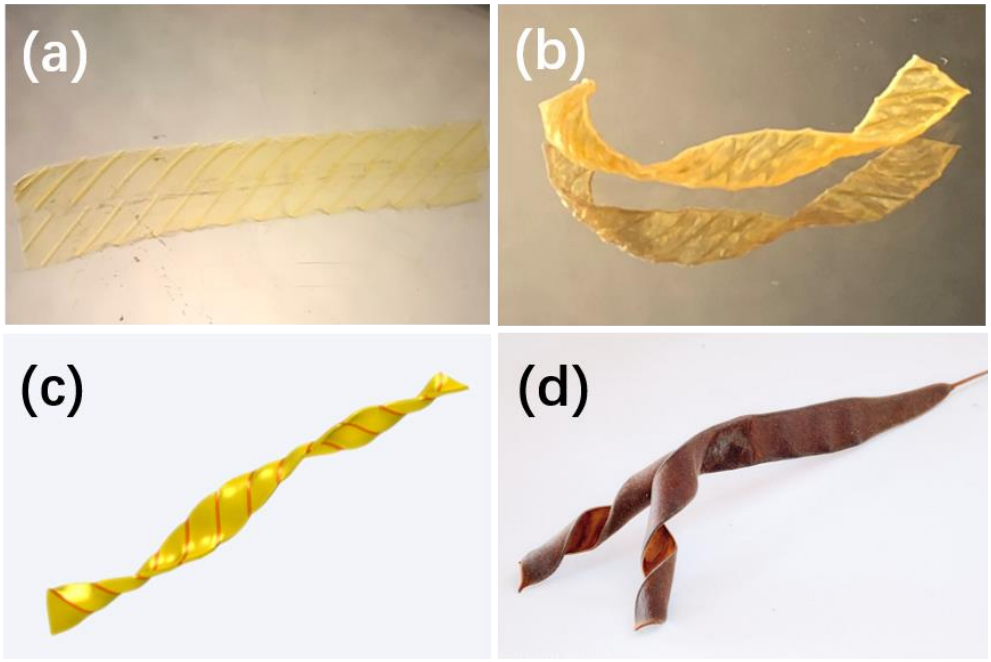

Figure 3.13 (a) the initial plain state; (b) the final buckling state; (c) the corresponding simulated models; and (d) the real images of helix strips of Bauhinia pods (p). (scale bar is 5mm)

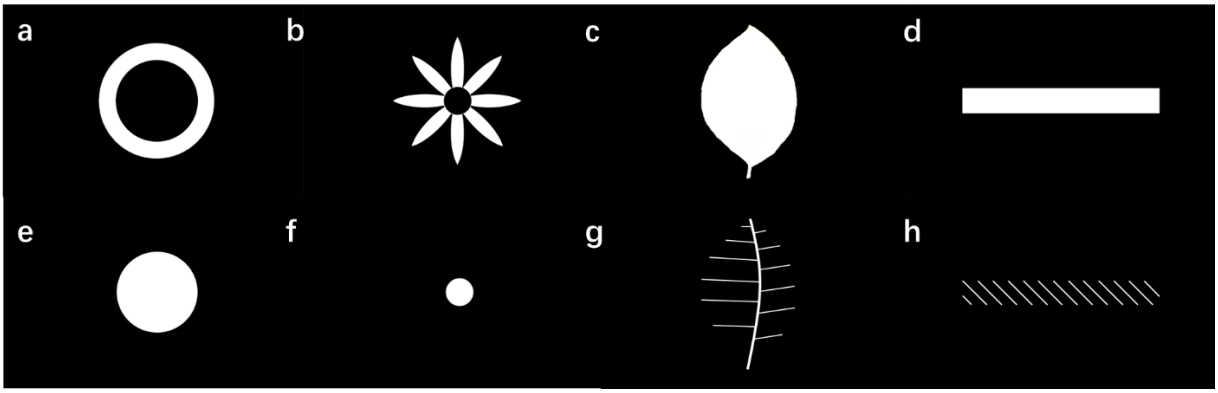

Figure 3.14. Projected patterns of different biomimetic structures: (a) core and (e) shell structure mimicking cabbage flowers/leaves; (b) petals and (f) core of chrysanthemum; (c) mesophyll and (g) veins of leaves of rose; (d)strip and (h) ridges of helix strips of Bauhinia pods.

As for the printing method of different 4D process, 2D flat sheets were printed, rinsed with ethanol and then immersed in buffer solution to mimic the morphologic formation of four different plants. A thin disk with 3s-cured shell (Figure 3.14 a) and 10s-cured core (Figure 3.14 e) was printed to lead to wave-like shape mimicking cabbage leaves. Structure with rigid core (Figure 3.14 f) and double-layer petals (Figure 3.14 b) was printed to mimic chrysanthemum. Rigid lines and curves within soft matrixes were printed to mimic leaves of rose and Bauhinia pods.

3.6 Simulation of 4D Process (with Zirui Zhai)

3.6.1 Theory of the Finite Element Analysis

The shape transition of hydrogels is a transient multi-physics process, which involves mass diffusion of water into/out of the gel and large deformation of the gel network. To model this

complicated behavior, the inhomogeneous field theory that couples large deformation and mass diffusion developed by Hong et al.[31] and the finite element method developed by Wang et al.[32] were used and implemented in the environment of commercial multi-physics modeling software COMSOL.

In the inhomogeneous field theory of gel, a standard approach in continuum mechanics is used for the kinematics of the network. The stress-free dry gel state is taken as the reference state. In large deformation, deformation gradient

$$\mathbf{F} = \frac{\partial \mathbf{x}(\mathbf{X}, t)}{\partial \mathbf{X}}$$

is used to map between the reference state (with coordinate **X**) and the current state (with coordinate **x**(**X**, *t*)).

For mass diffusion, the conservation of mass can be expressed as

$$\frac{\partial C}{\partial t} + \frac{\partial J_K}{\partial X_K} = 0 ,$$

where *C* is the nominal solvent concentration, and **J** is the nominal flux. An equivalent way to express the flux is through the true flux j_i

$$j_i n_i da = J_K N_K DA ,$$

where $n_i da$ is the element area in the current state deformed from its counterpart $N_K DA$ in the reference state. Using the conservation of mass in an integration form,

$$\frac{d}{dt}\int_V CdV + \int_A J_K N_K dA = 0,$$

and divergence theorem, the differential form in true flux can be expressed as

$$\frac{1}{\det \mathbf{F}}\frac{\partial C}{\partial t} + \frac{\partial j_i}{\partial x_i} = 0.$$

The nominal concentration *C* relates to the deformation via the condition of incompressibility

$$1 + \nu C = \det \mathbf{F},$$

and true concentration of solvent relate to the nominal concentration via

$$c \det \mathbf{F} = C.$$

The true flux is given by the gradient of the chemical potential,

$$j_i = -cD(T)\frac{\partial \mu}{\partial x_i}$$

Where *D(T)* is the temperature dependent intrinsic diffusivity and □ is the normalized chemical potential (by $k_B T$) of the solvent inside the gel. Thus the conservation of mass can be derived as

$$\frac{1}{\det \mathbf{F}}\frac{\partial(\det \mathbf{F} - 1)}{\partial t} + \frac{\partial\left[-\frac{(\det \mathbf{F} - 1)D(T)}{\det \mathbf{F}}\frac{\partial \mu}{\partial x_i}\right]}{\partial x_i} = 0$$

This equation can be directly implemented using the heat transfer equation or coefficient form of the PDE interface of COMSOL.

A user-defined hyper-elastic material node under solid mechanics interface can be used to describe the constitutive relation. One choice of the free energy density is the Flory-Huggins model, where the normalized nominal free energy density $\hat{W}(\mathbf{F})$ is given by[31]

$$\hat{W}(\mathbf{F}) = \frac{W(\mathbf{F},C)}{\frac{k_B T}{\nu}} = \frac{1}{2} N\nu \left[F_{iK} F_{iK} - 3 - 2\log(\det \mathbf{F}) \right] - \left[(\det \mathbf{F} - 1)\log\left(\frac{\det \mathbf{F}}{\det \mathbf{F} - 1} \right) + \frac{\chi}{\det \mathbf{F} - 1} \right] - \mu(\det \mathbf{F} - 1)$$

where $N\nu$ is a dimensionless materials property representing the shear modulus of the dry polymer and ν is molecule volume of water. The shear modulus of the dry polymer Nk_BT is related to the normalized shear modulus by $Nk_BT = \frac{k_BT}{\nu} N\nu$. T is the temperature, k_B is the Boltzmann constant and χ is the temperature dependent dimensionless materials properties representing the enthalpy of mixing, which can be determined by the experiment. With the solid mechanics and the PDE interface of COMSOL, the transient analysis of the gels with coupled mass diffusion and large deformation can now be formed. More details of this implementation can be found.[31-33]

3.6.2 2D Instability Simulation of Pumpkin Growth

To simplify the modeling of Pumpkin and focus on the instability phenomenon, a 2D plane stress condition is assumed here. It is also assumed that a surface energy is associated with the free boundary of the gel[33], which creates a surface traction $\vec{t}$ in the current configuration a

$$\vec{t} = t_0 \cdot \vec{n}$$

where $\vec{n}$ is the outer unit vector associated with the free boundary, and t_0 is set as 0.02 N/m for all the 2D instability simulations. The surface traction is applied after the gel system is fully swelled. The outer boundary is set as no displacement restriction and zero chemical potential. The displacement and chemical potential fields have continued values between the two layers of gels. Hundreds of quadratic elements have been used for both displacement and chemical potential field discretization.

3.6.3 3D Growing Simulations

The hydrogels are modeled with real dimensions of the dry gel states. Thousands of linear elements have been used for both displacement and chemical potential field discretization. All the outer boundaries are without displacement restriction and at zero chemical potential. The displacement and chemical potential fields have continued value between different gels. Because of geometric symmetry, 1/8 of the model is used for the simulation of the flower.

Table 3.1 Parameters used in the simulation

Parameter	**Description**	**Value**
ρ_{drygel}	Density of dry gel	
ρ_{water}	Density of water	1000 kg·m^{-3}
T	Water temperature	293.15 K
k_B	Boltzmann constant	$1.38064852\times10^{-23}\,\mathrm{J\cdot K^{-1}}$
v_{water}	Molecular volume of water	$2.99\times10^{-29}\,\mathrm{m^3}$
ν_{drygel}	Poisson's ratio of dry gel	0.5

E_{3s}	Young's modulus of 3 s dry gel	9 kPa
$E_{3.5s}$	Young's modulus of 3.5 s dry gel	23.8 kPa
E_{4s}	Young's modulus of 4 s dry gel	38.6 kPa
E_{8s}	Young's modulus of 8 s dry gel	186 kPa
E_{10s}	Young's modulus of 10 s dry gel	295 kPa
λ_{3s}	Length swelling ratio of 3 s dry gel	1.77
$\lambda_{3.5s}$	Length swelling ratio of 3.5 s dry gel	1.73
λ_{4s}	Length swelling ratio of 4 s dry gel	1.70
λ_{8s}	Length swelling ratio of 8 s dry gel	1.40
λ_{10s}	Length swelling ratio of 10 s dry gel	1.37

4. Conclusion

In summary, 3D longitudinal buckles are generated directly on the 3D curved surface to mimic morphogenesis of Cucurbita species' fructification. Number of the buckles are controlled easily through the printing procedure. Underlying mechanism of the pattern formation is revealed to achieve different biological behavior in morphogenesis.

Thanks to additive manufacturing technology with stimulus-responsive hydrogel, complex heterogeneous 3D structures were fabricated. Swelling ratio and the stiffness of the complex materials are easily tuned by the projection time in printing process, thus buckle number are controlled from 4 to 44 based on these two properties. Our core-shell model presents a different perspective of the buckling formation on the surface of Cucurbita species. The mechanism of the controllable buckle were applied to mimic different 4D behavior like leaf bending, flower blossom, Bauhinia pods helix and etc.

The experimental results of the morphology evolution from a 3D object (rather than from 2D flat sheet) also feed the development of long-sought theories of three-dimensional instability. We are the first to achieve ordered close-packed patterns directly on 3D surface by 4D printing method. In the following, these longitudinal buckles are expected to increase anti-bending capability for a 3D subject, and have potential applications such as 3D anti-counterfeiting films.

References

[1] S. Tibbits, The emergence of “4D printing”, http://www.ted.com/talks/skylar_tibbits_the_ emergence _of_4d_ printing.

[2] Q. Ge, H. J. Qi, M. L. Dunn, Active materials by four-dimension printing, *Appl. Phys. Lett.* **2013**, 103, 131901.

[3] S. Tibbits, 4D Printing: Multi-Material Shape Change, *Archit. Des.* **2014**, 84, 116.

[4] A. S. Gladman, E. A. Matsumoto, R. G. Nuzzo, L. Mahadevan, J. A. Lewis, Biomimetic 4D printing, *Nat. Mater.* **2016**, 15, 413.

[5] Z. Ding, O. Weeger, H. J. Qi, M. L. Dunn, 4D rods: 3D structures via programmable 1D composite rods, *Mater. Des.* **2018**, 137, 256.

[6] X. Kuang, D. J. Roach, J. Wu, C. M. Hamel, Z. Ding, T. Wang, M. L. Dunn, and H. J. Qi, Advances in 4D Printing: Materials and Applications, *Adv. Funct. Mater.* **2019**, 29, 1805290.

[7] F. Momeni, S. M. Mehdi, N. Hassani, X. Liu, J. Ni, A Review on 4D Printing Material Composites and Their Applications, *Mater. Des.* **2017**, 122, 42.

[8] B. Gao, Q. Yang, X. Zhao, G. Jin, Y. Ma, F. Xu, 4D bioprinting for biomedical applications, *Trends Biotechnol.* **2016**, 34, 746.

[9] Z. L. Wu, M. Moshe, J. Greener, H. Therien-Aubin, Z. Nie, E. Sharon, E. Kumacheva, Three-dimensional shape transformations of hydrogel sheets induced by small-scale modulation of internal stresses, *Nat. Commun.* **2013**, 4, 1586.

[10] H. Wei, Q. Zhang, Y. Yao, L. Liu, Y. Liu, J. Leng, Direct-write fabrication of 4D active shape-changing structures based on a shape memory polymer and its nanocomposite, *ACS Appl. Mater. Interfaces* **2017**, 9, 876.

[11] J. Wu, Z. Zhao, X. Kuang, C. M. Hamel, D. Fang, H. J. Qi, Reversible shape change structures by grayscale pattern 4D printing, *Multifunct. Mater.* **2018**, 1, 015002.

[12] K. Malachowski, J. Breger, H. R. Kwag, M. O. Wang, J. P. Fisher, F. M. Selaru, D. H. Gracias, Stimuli-responsive theragrippers for chemomechanical controlled release, *Angew. Chem.* **2014**, 126, 8183.

[13] J. Yin, X. Chen, I. Sheinman, Anisotropic buckling patterns in spheroidal film/substrate systems and their implications in some natural and biological systems, *J. Mech Phy. Solids* **2009**, 57, (9), 1470-1484.

[14] J. Dervaux, M. B. Amar, Morphogenesis of Growing Soft Tissues, *Phy. Rev. Lett.* **2008**, 101, 068101.

[15] L. Jin, S. Cai, Z. Suo, Creases in soft tissues generated by growth, *Europhys. Lett.* **2011**, 95, 64002.

[16] A. S. Gladman, E. A. Matsumoto, R. G. Nuzzo, L. Mahadevan, J. A. Lewis, Biomimetic 4D printing, *Nat. Mat.* **2016**, 15, 413–418.

[17] J. Dervaux, Y. Couder, M. A. Guedeau-Boudeville, M. B. Amar, Shape Transition in Artificial Tumors: From Smooth Buckles to Singular Creases, *Phy. Rev. Lett.* **2011**, 107, 018103.

[18] H. Lee, J. Zhang, H. Jiang, N. X. Fang, Prescribed Pattern Transformation in Swelling Gel

Tubes by Elastic Instability, *Phy. Rev. Lett.* **2012**, 108, 214304.

[19] H. Lee, N.X. Fang, Micro 3D Printing Using a Digital Projector and its Application in the Study of Soft Materials Mechanics, *J. Vis. Exp.* **2011**, 69, e4457.

[20] T. Tallinen, J. Y. Chung, J. S. Biggins, L. Mahadevan, Gyrification from constrained cortical expansion, *Proc. Natl. Acad. Sci* **2014**, 111, 12667-12672.

[21] J. P. Kruth, M. C. Leu, T. Nakagawa, Progress in Additive Manufacturing and Rapid Prototyping, *CIRP Ann.* **1998**, 47, 525.

[22] R. Janusziewicz, J. R. Tumbleston, A. L. Quintanilla, S. J. Mecham, J. M. DeSimone, Layerless fabrication with continuous liquid interface production, *Proc. Natl. Acad. Sci. USA* **2016**, 113, 11703.

[23] J. R. Tumbleston, D. Shirvanyants, N. Ermoshkin, R. Janusziewicz, A. R. Johnson, D. Kelly, K. Chen, R. Pinschmidt, J. P. Rolland, A. Ermoshkin, E. T. Samulski, J. M. DeSimone, Additive manufacturing. Continuous liquid interface production of 3D objects, *Science* **2015**, 347, 1349.

[24] J.-W. Choi, E. MacDonald, R. Wicker, Multi-material micro-stereolithography**,** *Int. J. Adv. Manuf. Technol.* **2010**, 49, 543.

[25] C. Sun, N. Fang, D. Wu, X. Zhang, Projection micro-stereolithography using digital micro-mirror dynamic mask, *Sens. Actuators A* **2005**, 121, 113.

[26] Z. Ding, C. Yuan, X. Peng, T. Wang, H. J. Qi, M. L. Dunn, Direct 4D printing via active composite materials, *Sci. Adv.* **2017**, 3, e1602890.

[27] A. Kotikian, R. L. Truby, J. W. Boley, T. J. White, J. A. Lewis, 3D Printing of Liquid Crystal Elastomeric Actuators with Spatially Programed Nematic Order, *Adv. Mater.* **2018**, 30, 1706164.

[28] H. Yang, W. R. Leow, T. Wang, J. Wang, J. Yu, K. He, D. Qi, C. Wan, X. Chen, 3D Printed Photoresponsive Devices Based on Shape Memory Composites, *Adv. Mater.* **2017**, 29, 1701627.

[29] O. Kuksenok, A. C. Balazs, Stimuli-responsive behavior of composites integrating thermo-responsive gels with photo-responsive fibers, *Mater. Horiz.* **2016**, 3, 53.

[30] M. Nadgorny, Z. Xiao, C. Chen, L. A. Connal, Three-Dimensional Printing of pH-Responsive and Functional Polymers on an Affordable Desktop Printer, *ACS Appl. Mater. Interfaces* **2016**, 8, 28946.

[31] W. Hong, X. Zhao, J. Zhou, Z. Suo, A theory of coupled diffusion and large deformation in polymeric gels, *Jour. Mech. Phys. Solids* **2008**, 56, 1779-1793.

[32] X. Wang, Z. Zhai, Y. Chen, H. Jiang, A facile, robust and versatile finite element implementation to study the time-dependent behaviors of responsive gels, *Extra. Mech. Lett.* 2018, 22, 89-97.

[33] Z. Duan, J. Zhang, Y. An, and H. Jiang, Simulation of the transient behavior of gels based on an analogy between diffusion and heat transfer, *Jour. Appl. Mech.* **2013**, 80, 041017.

[34] Y. Mao, Z. Ding, C. Yuan, S. Ai, M. Isakov, J. Wu, T. Wang, M. L. Dunn, H. J. Qi, 3D Printed Reversible Shape Changing Components with Stimuli Responsive Materials, *Sci. Rep.* **2016**, 6, 24761.

[35] T. van Manen, S. Janbaz, A. A. Zadpoor, Programming 2D/3D shape-shifting with hobbyist 3D printers, *Mater. Horiz.* **2017**, 4, 1064.

[36] J. Boothby, T. Ware, Dual-responsive, shape-switching bilayers enabled by liquid crystal elastomers, *Soft Matter* **2017**, 13, 4349.

[37] X. Kuang, K. Chen, C. K. Dunn, J. Wu, V. C. Li, H. J. Qi, 3D Printing of Highly Stretchable, Shape-Memory, and Self-Healing Elastomer toward Novel 4D Printing, *ACS Appl. Mater. Interfaces* **2018**, 10, 7381.

[38] Q. Ge, A. H. Sakhaei, H. Lee, C. K. Dunn, N. X. Fang, M. L. Dunn, Multimaterial 4D Printing with Tailorable Shape Memory Polymers, *Sci. Rep.* **2016**, 6, 31110.

[39] Z. Zhao, X. Kuang, C. Yuan, H. J. Qi, D.-N. Fang, Hydrophilic/Hydrophobic Composite Shape-Shifting Structures, *ACS Appl. Mater. Interfaces* **2018**, 10, 19932

[40] Z. Zhao, J. Wu, X. Mu, H. Chen, H. J. Qi, D. Fang, Desolvation Induced Origami of Photocurable Polymers by Digit Light Processing, *Macromol. Rapid Commun.* **2017**, 38, 1600625.

[41] J. Wu, Z. Zhao, X. Kuang, C. M. Hamel, D. Fang, H. J. Qi, Reversible shape change structures by grayscale pattern 4D printing, *Multifunct. Mater.* **2018**, 1, 015002.

[42] G. I. Peterson, J. J. Schwartz, D. Zhang, B. M. Weiss, M. A. Ganter, D. W. Storti, A. J. Boydston, Production of Materials with Spatially-Controlled Cross-Link Density via Vat Photopolymerization, *ACS Appl. Mater. Interfaces* **2016**, 8, 29037.

[43] J. Yin, Z. Cao, C. Li, I. Sheinman, X. Chen, Stress-driven buckling patterns in spheroidal core/shell structures, *Proc. Natl. Acad. Sci. USA* **2008**, 105, 19133.